JGR Solid Earth

RESEARCH ARTICLE
10.1029/2021JB023616

Key Points:

- Microstructures capable of recording transient stress changes prior to and during earthquake rupture in the lower crust
- Localized differential stresses exceeding 1 GPa during prerupture loading accommodated in dislocation glide of pyroxenes
- Coseismic deformation represented by pulverization style fragmentation and thermally activated grain growth within orthopyroxene

Supporting Information:

Supporting Information may be found in the online version of this article.

Correspondence to:

L. R. Campbell,
l.r.campbell@hull.ac.uk

Citation:

Campbell, L. R., & Menegon, L. (2022). High stress deformation and short-term thermal pulse preserved in pyroxene microstructures from exhumed lower crustal seismogenic faults (Lofoten, Norway). *Journal of Geophysical Research: Solid Earth*, *127*, e2021JB023616. https://doi.org/10.1029/2021JB023616

Received 19 NOV 2021
Accepted 5 JUL 2022

Author Contributions:

Conceptualization: L. R. Campbell, L. Menegon
Formal analysis: L. R. Campbell, L. Menegon
Funding acquisition: L. Menegon
Investigation: L. R. Campbell, L. Menegon
Project Administration: L. R. Campbell, L. Menegon
Supervision: L. Menegon
Writing – original draft: L. R. Campbell
Writing – review & editing: L. R. Campbell, L. Menegon

High Stress Deformation and Short-Term Thermal Pulse Preserved in Pyroxene Microstructures From Exhumed Lower Crustal Seismogenic Faults (Lofoten, Norway)

L. R. Campbell[1] and L. Menegon[2]

[1]Department of Geography, Geology and Environment, University of Hull, Hull, UK, [2]The Njord Centre, Department of Geosciences, University of Oslo, Oslo, Norway

Abstract Earthquake rupture in strong, anhydrous lower continental crust requires high brittle failure stresses unless high pore fluid pressures are present. Several mechanisms proposed to generate high stresses at depth imply transient loading driven by a spectrum of stress changes, ranging from highly localized stress amplifications to crustal-scale stress transfers. High transient stresses up to GPa magnitude are proposed by field and modeling studies, but the evidence for transient prerupture loading is often difficult to extract from the geological record due to overprinting by coseismic damage and slip. However, the local preservation of deformation microstructures indicative of crystal-plastic and brittle deformation associated with the seismic cycle in the lower crust offers the opportunity to constrain the progression of deformation before, during and after rupture, including stress and temperature evolution. Here, detailed study of pyroxene microstructures characterizes the short-term evolution of high-stress deformation and temperature changes experienced before and during lower crustal earthquake rupture. Pyroxenes are sampled from pseudotachylyte-bearing faults and damage zones of lower crustal earthquakes recorded in the exhumed granulite facies terrane of Lofoten, northern Norway. The progressive sequence of microstructures indicates localized high-stress (at the GPa level) prerupture loading accommodated by low-temperature plasticity, followed by coseismic pulverization-style fragmentation and subsequent grain growth triggered by the short-term heat pulse associated with frictional sliding. Thus, up to GPa-level transient high stress (both differential and shear) leading to earthquake nucleation in the dry lower crust can occur in nature, and be preserved in the fault rock microstructure.

Plain Language Summary Earthquake initiation within strong, dry rock types in the Earth's lower continental crust requires high driving stresses if fluids are absent. Several mechanisms have been proposed to generate these unusually high stresses deep in the lower crust, many of which imply very short-term stress increases. High short-term stresses are proposed by field-based studies and numerical modeling, but the geological record for these stress increases occurring in the build-up to earthquakes is not always obvious because the effects of the subsequent earthquake normally will overprint the evidence. However, in some cases a complete record of stress change before, during and after an earthquake may survive. In this study, detailed observations of the deformation of pyroxene (a silicate mineral) characterizes the short-term changes in stress and temperature experienced before and during earthquakes recorded in the lower crust. Pyroxene crystals close to faults exhibiting ancient earthquake-generated frictional melts (pseudotachylytes) are investigated from an exhumed fault zone in Lofoten, northern Norway. The microstructures imply high stress increases prior to the earthquake, followed by widespread fragmentation and grain growth linked to the passage of earthquake slip. These results support very high stresses localized within the lower crust and show that crystal deformation can capture such changes.

1. Introduction

Relocations of earthquakes, the study of focal mechanisms, and increased recognition of the geological signature of earthquakes recorded in exhumed lower crustal settings have promoted various models for nucleating seismic rupture within otherwise typically viscous deformation conditions. Many of these models require stress amplification or transfer, whether driven by local rheological heterogeneities across a shear zone network (Campbell et al., 2020; Hawemann et al., 2019; Orlandini & Mahan, 2020), dehydration reactions that increase fluid pressure (Hacker et al., 2003) or locally redistribute stress (Ferrand et al., 2017), or downdip stress loading from seismogenic activity shallower in the crust (Dunkel et al., 2020; Ellis & Stöckhert, 2004; Jamtveit et al., 2018; Okudaira

et al., 2015; Papa et al., 2020). Intracrystalline deformation and recrystallization occurring over geologically rapid timescales (i.e., equivalent to the seismic cycle) have been previously recognized in fault zones and deformation experiments (Bestmann et al., 2012; Campbell & Menegon, 2019; Kidder et al., 2016; Kim et al., 2010; Küster & Stöckhert, 1999; Trepmann & Stöckhert, 2001), and recent work on both naturally and experimentally deformed mid-to lower-crustal rocks has linked similar microstructures to stress transients. In some cases, such microstructures can be clearly linked to localized stress amplifications associated with deep crustal earthquakes, whether stress increases were generated in situ within the lower crust (Anderson et al., 2021; Campbell et al., 2020; Hawemann et al., 2019) or were transferred from shallower crustal levels (Ellis & Stöckhert, 2004; Papa et al., 2020; Trepmann & Stöckhert, 2002, 2013). In both cases the stress amplification can be significant within and just below the frictional-viscous transition zone (e.g., >300–500 MPa, Ellis & Stöckhert, 2004; Trepmann & Stöckhert, 2001; Brückner & Trepmann, 2021), but earthquake rupture of the lower crust may require stresses on the order of GPa, especially within strong, anhydrous granulites in the absence of high pore fluid pressure. Such stress magnitudes prior to rupture have been implied by field characterization of pseudotachylyte-bearing faults (Campbell et al., 2020) and, perhaps more commonly, are also associated with deformation linked to coseismic loading once rupture propagation has initiated (e.g., Anderson et al., 2021). This microstructural record of progressive and transient stress variation throughout the earthquake cycle (Anderson et al., 2021; Bestmann et al., 2012; Brückner & Trepmann, 2021; Campbell & Menegon, 2019; Johnson et al., 2021; Mancktelow et al., 2022; Petley-Ragan et al., 2019) offers an under-explored opportunity to further constrain deformation mechanisms and conditions associated with both prerupture stress amplification and coseismic rupture within the lower crust.

We present here a microstructural study of lower crustal pseudotachylyte-bearing faults that seeks to constrain the timing and magnitude of stresses associated with the nucleation and propagation of earthquake rupture within the lower crust, as well as the corresponding sequence of deformation processes. Following work on deformation of plagioclase (e.g., Soda & Okudaira, 2018; Petley-Ragan et al., 2018, 2021) and garnet (Austrheim et al., 2017; Hawemann et al., 2019; Papa et al., 2018; Petley-Ragan et al., 2019) in lower crustal seismogenic faults, we focus on the deformation microstructures of pyroxenes, which present a more explicit record relative to plagioclase of overprinting and spatial association of deformation with localized faulting in our samples. The spatial association of our samples with pseudotachylyte-bearing faults allows a direct link with earthquake rupture processes to be tested (e.g., Rowe & Griffith, 2015; Sibson, 1975). The structural setting for the sampled faults was characterized in Campbell et al. (2020). The pseudotachylyte-bearing faults nucleated at lower crustal depths under stress amplifications driven by local and coeval viscous shear zone activity, rather than requiring loading from shallower earthquake slip (although this in situ nucleation is still compatible with the potential presence of a seismically active upper crustal fault zone, Campbell et al., 2020). From field-based fault measurements, seismic scaling laws imply that the stress amplifications locally may have reached 1 GPa, but field evidence alone could not provide certainty for absolute stress constraints (Campbell et al., 2020). We adopt here a microstructural approach to constrain the deformation mechanisms and record of stress changes to address that uncertainty. By studying orthopyroxene and clinopyroxene both from the margins of, and as unmelted clasts within, granulite-facies pseudotachylyte-bearing faults, we propose a record of spatial and temporal stress and temperature variation related to the earthquake cycle in the lower continental crust.

2. Geological Context

We investigate pseudotachylyte samples from the Flakstadøy anorthosite near Nusfjord, Lofoten, Norway. This anorthosite body forms part of the Anorthosite-Mangerite-Charnockite-Granite (AMCG) suite, intruded into the Baltic Shield's lower crust around 1.9–1.7 Ga at granulite facies conditions (Corfu, 2004). The well-preserved coarse-grained igneous texture and mineralogy of the Flakstadøy anorthosite consists of plagioclase + minor amounts of clinopyroxene ± amphibole ± quartz ± orthopyroxene ± garnet ± biotite (Markl et al., 1998; Menegon et al., 2017). The anorthosite can be considered anhydrous, containing c. 0.04 wt. % H_2O and no free H_2O at the time of deformation (Menegon et al., 2017).

Within the Flakstadøy anorthosite, a network of thin shear zones (usually 1–30 cm in width) cut across the intrusion, occurring in three dominant orientations (Menegon et al., 2017) and dividing the anorthosite into low-strain blocks (Figures 1a and 1b). Some of these bounding shear zones contain mylonitized pseudotachylytes (classified as "type-1" pseudotachylytes by Campbell et al., 2020); these mylonitized pseudotachylytes are not considered

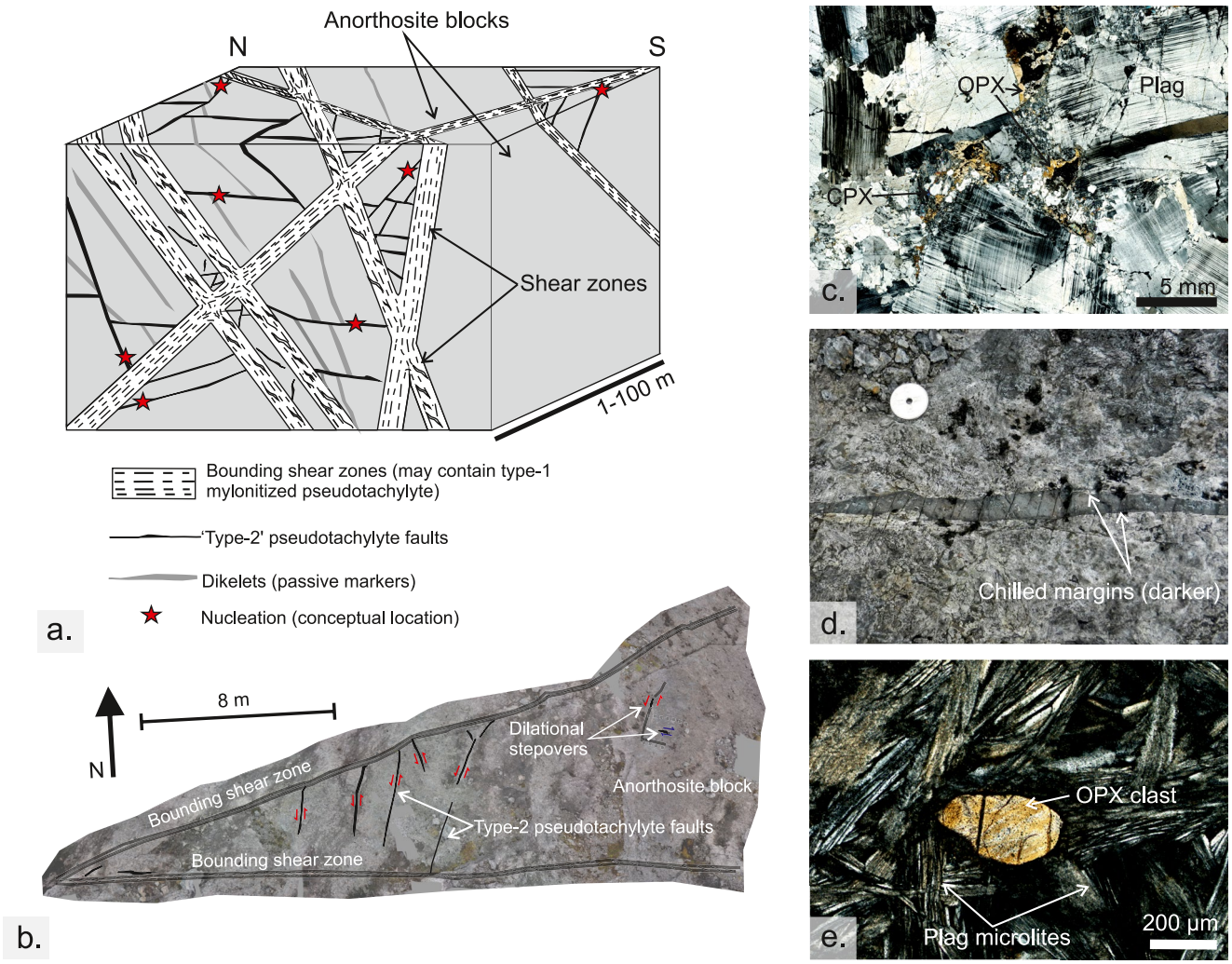

Figure 1. Pseudotachylytes representing lower crustal earthquake rupture associated with viscous creep along active shear zone networks near Nusfjord, Lofoten. (a) Block diagram showing pseudotachylyte faults that dissect low-strain anorthosite blocks between localized viscous shear zones (adapted from Campbell et al. (2020)). The small fault length and their restriction to anorthosite blocks between the shear zones is consistent with their coeval formation at the lower crustal conditions interpreted for viscous creep on the shear zones (Menegon et al., 2017); (b) map of faults and shear zones across one such block in the Flakstadøy anorthosite (68.055°N 13.367°E)—adapted from Campbell et al. (2020); (c) typical form of anorthosite within shear-zone bounded blocks at distance from pseudotachylyte faults. The plagioclase shows microfracturing but very limited evidence for viscous creep (cross-polarised image). (d) example of pseudotachylyte fault with chilled margin located in block shown in (b) (68.055°N 13.367°E); (e) Orthopyroxene ("OPX") clast in crystalline matrix of pseudotachylyte showing characteristic radiating plagioclase ("Plag") microlites (cross-polarised image).

further in the present study. However, between the bounding shear zones and within the otherwise low-strain blocks, pristine, mylonitized pseudotachylyte vein networks are observed—classified as "type-2" pseudotachylytes by Campbell et al. (2020). Along the length of these veins, offset of passive markers and/or typical fault geometries such as dilational stepovers (Campbell et al., 2020) indicate that they represent fault veins that localized slip, and not large injection veins (i.e., Mode I fractures). The earthquakes recorded by these type-2 veins are estimated to have had approximate magnitudes of M_W 0.2–2.6 (Campbell et al., 2020). The surrounding anorthosite, while fractured, also typically shows only minimal evidence of viscous creep away from either the shear zones or the pseudotachylyte veins (Figure 1c).

The transient high stresses required to trigger brittle failure within these blocks were interpreted to result from localized stress amplification driven by activity along the viscously deforming shear zones (Campbell et al., 2020). Therefore, the earthquakes recorded by these "type-2" pseudotachylytes (Figure 1d) nucleated at the ambient conditions of the coeval shear zone deformation, 650–750°C and 0.7–0.8 GPa (Menegon et al., 2017), implying depths of 25–30 km in the continental lower crust. In this contribution, we evaluate the microstructural evidence

for these transient occurrences of GPa -magnitude prerupture loading suggested by Campbell et al. (2020) and identify further coseismic rapid stress and temperature oscillations.

3. Materials and Methods

3.1. Sampling Choice and Location

Samples were sourced from pseudotachylyte veins cutting across ~10 m blocks of anorthosite separated from the adjacent blocks by shear zones (Figure 1a). Mylonitised pseudotachylytes found along many of the bounding shear zones ("type-1" pseudotachylytes) are not considered in the present study since any microstructural record related to pre- and coseismic deformation has been overprinted by subsequent viscous creep. Between the shear zones, pseudotachylyte veins cut across the anorthosite, and these typically lack pervasive viscous overprint, instead preserving primary quench crystallization morphologies (e.g., radiating microlites, spherulites, dendritic crystals) and chilled margins (Figures 1d and 1e) that reflect extremely rapid crystallization from a melt. These pseudotachylyte veins ("type-2 pseudotachylytes") show clear evidence of being fault veins rather than injection veins, displaying dilational pull-aparts in stepover geometries and offset of passive markers consisting of dikelets or older pseudotachylyte-bearing faults. These pseudotachylyte veins have mean vein thicknesses of 1–10 mm, and measured displacements range from 1 to 26 cm along fault lengths of 1.9–11.1 m (Campbell et al., 2020). These type-2 pseudotachylytes are considered to record single-slip faulting (i.e., a single earthquake) with nucleation at lower crustal depths (Campbell et al., 2020).

Samples N22 and LC1724 included in this study belong to two different networks of short (<15 m long) type-2 pseudotachylyte-bearing faults developed in decametric pods of undeformed anorthosite bounded by ductile shear zones (Figures S1a and S1b in Supporting Information S1). These fault systems share several of the defining characteristics of the type-2 pseudotachylyte networks described in detail in Campbell et al. (2020). N22 was sampled from 68.055°N 13.367°E (Figure 1b) and LC1724 from 68.056°N 13.377°E (Figure S1a in Supporting Information S1). Both samples come from fault-vein networks with localized slip, as indicated by truncated passive markers and/or pull-aparts along their strike (Figures S1c and S1d in Supporting Information S1).

Two near-parallel SE-dipping bounding shear zones characterize the LC1724 sampling site, with a type-2 network of NE-, ESE- and SE- dipping pseudotachylyte-bearing faults cutting across the 6–10 m wide anorthosite block in between (Figures S1b and S1e in Supporting Information S1). Type-2 faults at this site show similar orientations (Figures S1e and S1f in Supporting Information S1) to similar type-2 networks analyzed in Campbell et al. (2020).

N22 (Figure 1d) was sampled from a type-2 pseudotachylyte found in a block bounded by two near-parallel SE-dipping shear zones. The N22 fault vein dips steeply to the NNW and is 4 m long. No offset markers were found along strike, but a 5-cm wide pull-apart structure indicates sinistral slip (Figure S1d in Supporting Information S1).

3.2. Microstructural Analysis and Electron Backscatter Diffraction (EBSD)

Four sections from two samples (N22 and LC1724) of pseudotachylyte veins were cut perpendicular to the vein walls (Figure 2) but the true slip direction within the sample remains unconstrained. Thin sections were analyzed using a combination of light and scanning electron microscopy (SEM). SEM data were acquired at the Electron Microscopy Centre at the University of Plymouth using a JEOL 7001 FEG-SEM and a JEOL 6610 low vacuum SEM. Typical beam conditions were 10–13 nA probe current and 20 kV accelerating voltage.

Samples for electron backscatter diffraction (EBSD) analysis underwent additional preparation with colloidal silica polishing and carbon coating. Data were acquired at the Electron Microscopy Centre at the University of Plymouth using a JEOL 7001 FEG-SEM and a JEOL 6610 low vacuum SEM, equipped with an Oxford Instruments Nordlys Nano and a Nordlys Max detector, respectively. During EBSD analysis, working distances were between 15.2 and 24.2 mm, accelerating voltage was 20 kV, and the sample was tilted at 70°. Step sizes for EBSD mapping ranged from 0.1 to 0.9 μm. Phases were indexed using AZtec (Oxford Instruments) acquisition software. Processing was undertaken with Channel 5 (Oxford Instruments) software. Filtering of the raw data involved removing noise, nearest neighbor extrapolation and removal of any grains with circle-equivalent diameters less than three times the step size. The results are presented in the form of phase maps, orientation maps (inverse pole

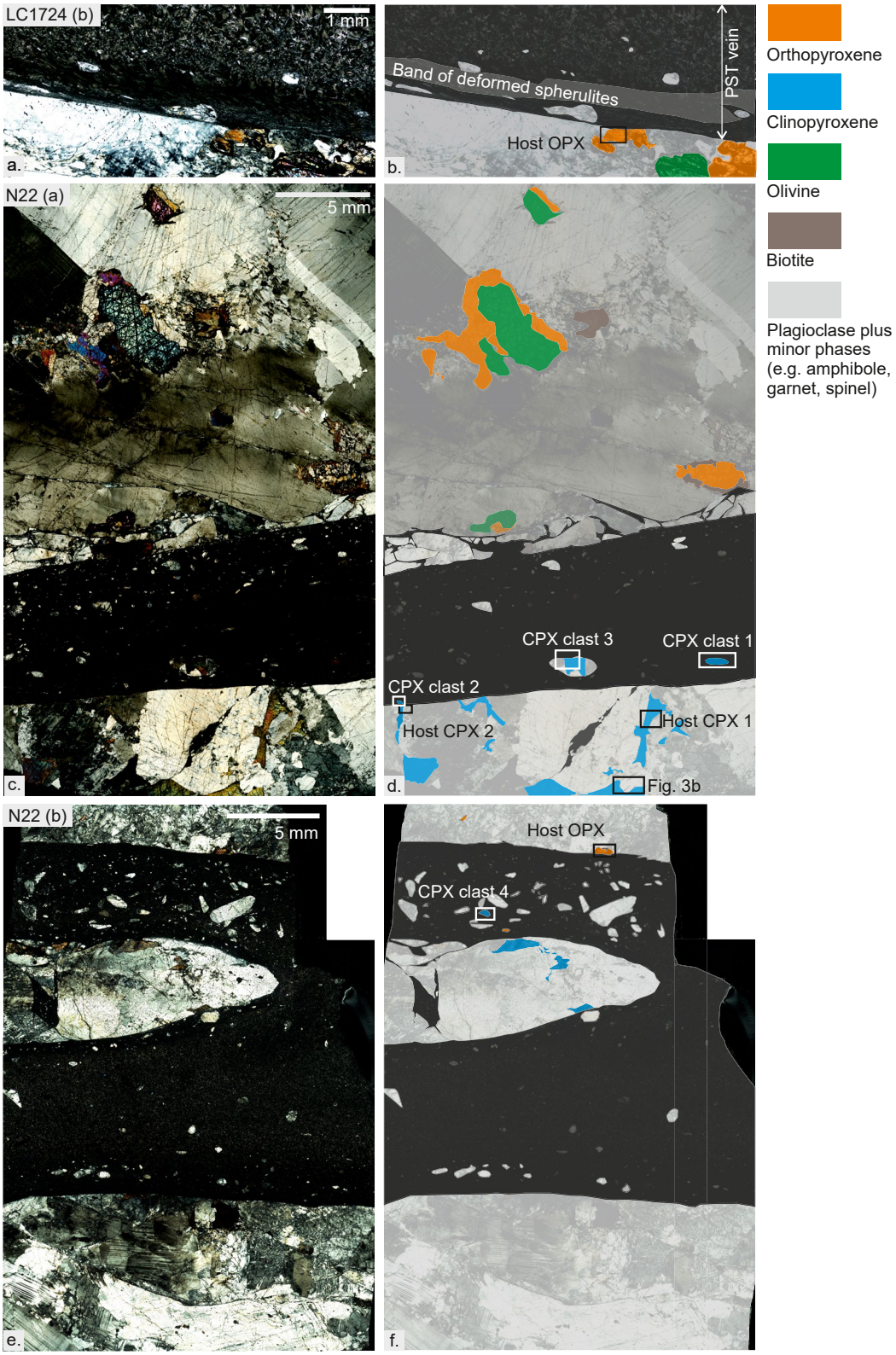
LC1724 (b)
1 mm
a.
Band of deformed spherulites
PST vein
Host OPX
b.
N22 (a)
5 mm
c.
CPX clast 3
CPX clast 1
CPX clast 2
Host CPX 2
Host CPX 1
Fig. 3b
d.
N22 (b)
5 mm
e.
Host OPX
CPX clast 4
f.
Orthopyroxene
Clinopyroxene
Olivine
Biotite
Plagioclase plus minor phases (e.g. amphibole, garnet, spinel)

Figure 2.

figure, IPF, maps), grain orientation spread (GOS) maps, showing the average misorientation of a grain with respect to that grain's mean orientation, grain reference orientation deviation maps, showing the misorientation of points relative to that grain's mean orientation, and texture component (TC) maps showing the misorientation with respect to a chosen reference point within the grain. Pole figures (lower hemisphere, equal angle) and maps are orientated with respect to the pseudotachylyte vein and pole figures show a reference frame perpendicular (Z_v) and parallel (X_v) to the vein edge.

3.3. Boundary Trace Analysis

Identification of slip systems using EBSD analysis was undertaken using the boundary trace analysis (BTA) technique. Using this technique, subsetted regions transecting low-angle boundaries (with misorientation in the 3–10° range) were created from EBSD orientation maps. Pole figures were created for each subset. The BTA method assumes a tilt boundary model, where the two regions on each side of the boundary are rotated around an axis lying within the boundary plane. This axis, if parallel to a crystal axis, will be represented in the pole figure by a tight point cluster at the position of that axis, while the other crystal axes may show rotation around that orientation via a dispersed smear of points. The slip plane can be identified as it must contain both the rotation axis and the slip direction, and the slip direction along with the pole to the slip plane must lie in a plane that is perpendicular to the rotation axis (Lloyd et al., 1997).

3.4. Image Analysis for Gain Size Distributions

Analysis of grain-size distributions of fine-grained pyroxene aggregates occurring in the damage zone of and in survivor clasts within type-2 pseudotachylytes was undertaken using the freely available image analysis software "ImageJ." Grain boundaries were identified via segmentation of SEM backscatter electron (BSE) images acquired at magnification ranging from 850x to 2300x. This magnification was sufficient to resolve the fractures and grain boundaries in the areas of interest (Campbell & Menegon, 2021). Grain area and circle equivalent diameter (D_{equ}) were measured and calculated using ImageJ software.

4. Results

4.1. Sample Characterization

Pyroxenes are described from two pseudotachylyte veins: LC1724 (Figures 2a and 2b) and N22 (Figures 2c–2f). These veins both show grain size reduction toward the margins of the vein. In sample LC1724, restricted viscous shear deformation is observed in the fine-grained pseudotachylyte margin (Figure 2a; Figure S2 in Supporting Information S1). However, this observation is restricted to a zone <1 mm wide adjacent to the margin, and has not deformed the fault walls of the anorthosite (Figure S2 in Supporting Information S1).

The anorthosite host rock in these samples consists of plagioclase (labradorite), clinopyroxene (diopside) and orthopyroxene (enstatite), with minor amounts of olivine, hornblende, biotite, pleonaste spinel, and garnet (Figure 2). Olivine is fractured and mostly altered to iron oxides and enstatite and is locally rimmed by coronas of intergrown enstatite, pleonaste spinel, hornblende, and biotite. Garnet may rim orthopyroxene in contact with plagioclase.

The microcrystalline matrix of the LC1724 pseudotachylyte is primarily composed of plagioclase (labradorite), orthopyroxene (enstatite) and clinopyroxene (diopside). Locally the pseudotachylyte matrix may also contain biotite, potassium feldspar and hornblende. The pseudotachylyte vein displays radiating elongate microlites of plagioclase in the center of the vein but these become finer and more granular toward the margin (Figures 1e and 2a). Clasts observed in this sample are composed predominantly of plagioclase and orthopyroxene. The margin with the host rock is planar and has no significant injection features visible within the thin section. The pseudotachylyte vein in the thin section is 11 mm thick.

Figure 2. Distribution of pyroxenes and other phases in association with pseudotachylyte veins. Areas analyzed in this work are labeled; (a) pseudotachylyte fault vein and anorthosite host rock in sample LC1724. (Only one side of the fault is captured—the margin of this pseudotachylyte vein has a 1 mm thick band of sinistrally sheared spherulitic structures (cross-polarised light, thin section "b"—see Figure S2 in Supporting Information S1 for details of margin); (b) overlay highlighting mineralogy of (a); (c) pseudotachylyte fault vein cutting anorthosite in sample N22 (cross-polarised light, thin section "a"); (d) overlay highlighting mineralogy in (c); (e) Thin section N22b (cross-polarised light) showing pseudotachylyte vein and clasts; (f) overlay showing mineralogy of (e).

The microcrystalline matrix of the N22 pseudotachylyte is composed of plagioclase (andesine), orthopyroxene (enstatite), clinopyroxene (diopside), hornblende and minor biotite (see Menegon et al. (2017) for XRF analysis of sample N22). Clasts are typically of plagioclase, orthopyroxene, clinopyroxene and some apatite. A damage zone containing fragmented wall rock surrounded by thin veins of pseudotachylyte extends for around 2 mm preferentially on one side of the main vein (Figures 2c and 2d). An additional sample of the N22 vein displays a large, cm-scale fragmented lithic clast with an internal network of thin pseudotachylyte injection veins connected to the main vein (Figure 2e). The main pseudotachylyte vein has a maximum thickness of 18 mm.

4.2. Microstructure of Clinopyroxene

4.2.1. Host Rock

Across the undeformed host rock, clinopyroxene grains display orthopyroxene lamellae. In the anorthosite internal blocks between shear zones (Figure 1a), clinopyroxene only rarely has twins evident (Figure 3a), but twins become common close to pseudotachylyte veins (Figure 3b) at distances of <2 cm (i.e., within a thin section).

EBSD maps of an elongate clinopyroxene grain (Figure 2d, "host CPX 1") lying 1–2 mm away from the N22 pseudotachylyte fault vein margin indicate laminar and slightly discontinuous twins on (001) and to some extent on (100) planes (Figures 3c–3e). (001) twins are cut by a probable fracture, here picked up as a low-angle boundary (LAB, misorientation of 3–10°) in Figure 3c (white lines). Not all LABs in the EBSD maps, however, necessarily represent fractures. Lamellae of orthopyroxene also lie along (100) planes of clinopyroxene. The grain orientation spread (GOS) of the clinopyroxene grain is <5° and is lowest within the twins (Figure 3d). Clinopyroxene in the immediate margin to the fault (Figure 2d, "host CPX 2"), and cut by the pseudotachylyte vein, shows laminar (001) twins (Figures 3f–3h). The GOS of the clinopyroxene grain here is variable but always <4° and again is lowest in the twin lamellae (Figure 3g). Although the IPF (Z) map is fairly uniform, grain reference orientation deviation maps pick out subtle undulations parallel to (001) (Figure S3a in Supporting Information S1).

4.2.2. Clasts in Pseudotachylytes

All clasts of clinopyroxene display twins on (100) and orthopyroxene lamellae along (100) (Figures 4 and 5). Clast 1 (Figure 2d, "clinopyroxene clast 1") is the most obviously elongate in shape (Figure 4), measuring approximately 1000 × 300 μm, but all other clasts appear slightly elongate parallel to the vein margin except for clast 3, where the clinopyroxene forms part of a lithic clast alongside plagioclase (Figure 2d, "CPX clast 3"). (100) is typically parallel or sub-parallel to the vein margin in clasts 1 and 3–4. Clast 1, and to some extent clast 4 (Figure 2f "CPX clast 4"), are bent, visible in the curvature of orthopyroxene lamellae (Figures 4 and 5c).

Clasts 1 and 4, plus regions near the edges of clasts 2 and 3 (Figures 2a and 2b) show moderately high GOS to 12° (Figures 4b, 5d and 5e). Lower GOS values are seen within twins and orthopyroxene lamellae, and the lowest values occur where the orthopyroxene lamellae have recrystallized into a polycrystalline aggregate. Clasts 1, 3, and 4 show systematic undulations with amplitudes of low misorientation (<4°) with wavelengths typically of 20–40 μm, which are most evident on texture component maps in regions free from twins and low-angle boundaries of 3–10° misorientation (Figures 4d and 5f). These features continue into the orthopyroxene lamellae. The change in orientation across these undulations is continuous (Figures 4f and 5g) and we use the term "periodic undulations" to refer to these. The boundary trace analysis in clast 1 indicates that the undulations are the result of slip on the [001] (100) system with [010] as the rotation axis (Figures 4g and 4h). However, the undulations in clast 4 do not give a clear rotation axis for boundary trace analysis, though there is some clustering around [001] (Figure 5h).

Low-angle boundaries are developed in different orientations, most clearly seen in clast 1, which displays them in at least three different orientations. Continuous linear LABs tend to correspond to fractures while shorter, branching LABs define a region of patchy short-scale misorientation development running diagonally upwards through the center of the clast (Figure 4). All LABs cut and offset the orthopyroxene lamellae and the periodic undulations. Clast 4 also has prominent linear LABs with some common orientations (Figure 5c). As in clast 1, some linear LABs cut the undulations and offset sharply the orthopyroxene lamellae (Figure 5f).

Fine-grained clinopyroxene occurs in intracrystalline bands across some clasts. In clast 2, fine-grained clinopyroxene has D_{equ} of 1.8–8.2 μm (Figure 5a), showing similar but dispersed orientations relative to the parent clast (Figure S4 in Supporting Information S1). The rotation axes of these smaller grains are scattered and do not

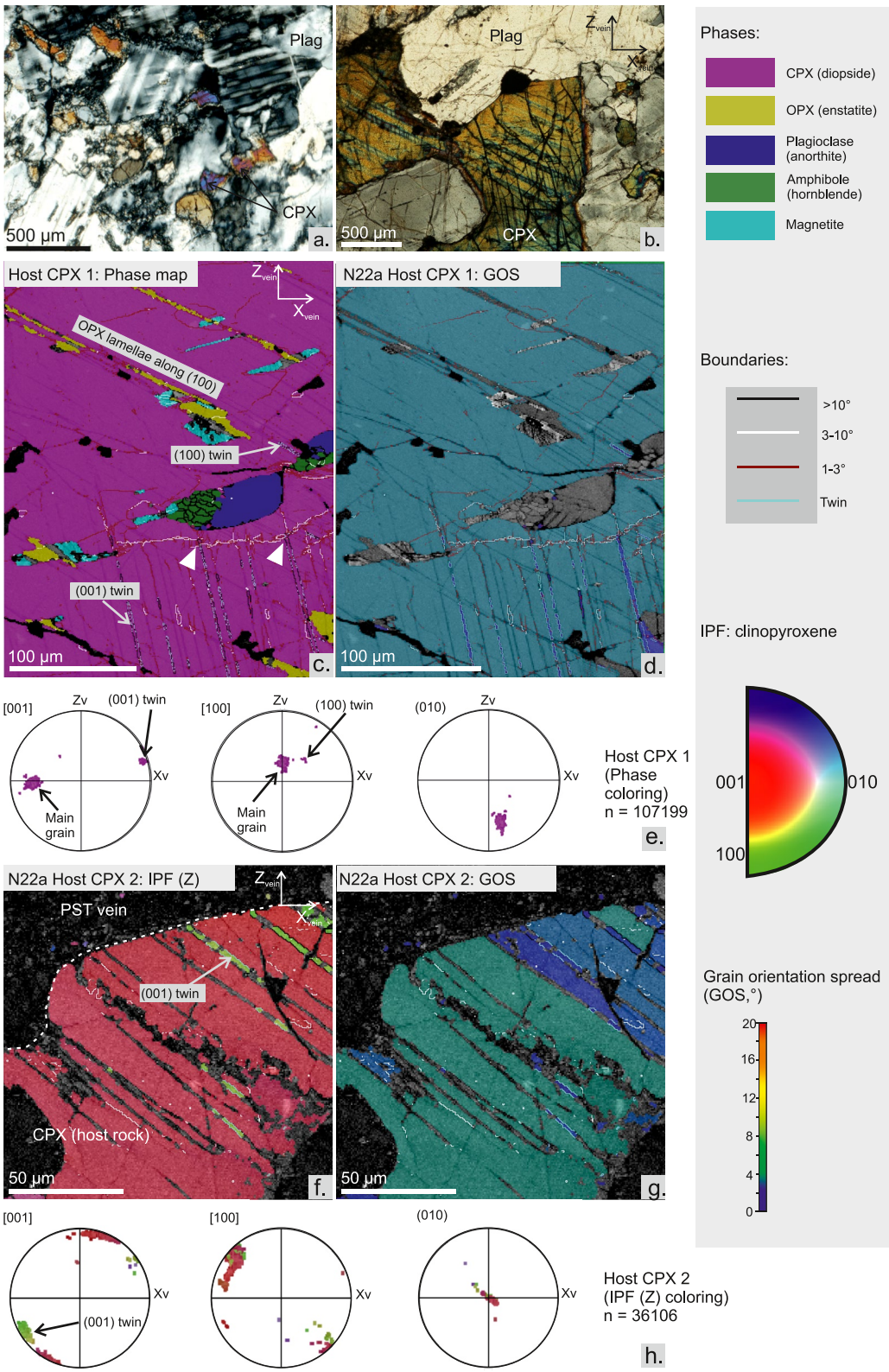
Plag
CPX
500 μm
a.
Plag
CPX
500 μm
b.
Phases:
CPX (diopside)
OPX (enstatite)
Plagioclase (anorthite)
Amphibole (hornblende)
Magnetite
Host CPX 1: Phase map
OPX lamellae along (100)
(100) twin
(001) twin
100 μm
c.
N22a Host CPX 1: GOS
100 μm
d.
Boundaries:
>10°
3-10°
1-3°
Twin
IPF: clinopyroxene
001
010
100
[001]
Zv
(001) twin
Xv
Main grain
[100]
(100) twin
[010]
Host CPX 1 (Phase coloring) n = 107199
e.
N22a Host CPX 2: IPF (Z)
PST vein
(001) twin
CPX (host rock)
50 μm
f.
N22a Host CPX 2: GOS
50 μm
g.
Grain orientation spread (GOS,°)
20
16
12
8
4
0
Host CPX 2 (IPF (Z) coloring) n = 36106
h.

Figure 3.

cluster around crystallographic rotation axes. The intracrystalline bands may also contain hornblende (Figure 5a), crosscut some LABs (Figure 5a), and generally offset orthopyroxene lamellae sharply. Clast 3 contains a similar example of a prominent intracrystalline band with a width up to 15 μm (Figure 5b). Fine-grained clinopyroxene in this band has a dispersed CPO relative to the rest of the clast (Figures S4c and S4d in Supporting Information S1). Orthopyroxene lamellae, clinopyroxene twin boundaries, and any LABs are truncated and offset across the band. The band contains fine-grained clinopyroxene alongside garnet and hornblende (Figure 5). Both are also fine-grained (2–20 μm), although the garnet coarsens at the edge of the mapped region, on the rim of the clinopyroxene grain. This assemblage shows no sign of retrograde metamorphic reactions relative to the estimated conditions of deformation (Menegon et al., 2017). Similar bands in clinopyroxene filled with fine-grained clinopyroxene and amphibole were described from the proximal damage zone of Nusfjord type-2 pseudotachylytes in Jamtveit et al. (2019), and were interpreted as intracrystalline fractures that localized mineral reactions and phase nucleation.

4.3. Microstructure of Orthopyroxene

4.3.1. Host Rock

Orthopyroxene in the host rock away from the pseudotachylyte veins does not display microstructural evidence of deformation, apart from weak to moderate undulose extinction. In the host rock at the immediate margin of the pseudotachylyte veins N22 and LC1724, the faults cut through orthopyroxene grains (Figures 2, 6 and 7). These fault-margin grains show a number of microstructures that are not seen in more distal orthopyroxenes.

In N22, most of the orthopyroxene grain on the margin is fractured (Figures 6a and 6b), but a transition is seen from linear fractures (e.g., Figure 6c) to a particularly fine-grained, pervasively fragmented regions (Figures 6d–6h). An orthopyroxene grain on the margin of the vein in LC1724 shows a similar feature (Figure S5 in Supporting Information S1). Within these fragmented regions, there is variation in grain size and shape between subdomains of fine-grained, fairly equant fragments (root-mean-squared grain diameter of 1.4 μm for N22, e.g., Figure 6f), adjacent regions of coarser grains (Figure 6e), and regions of larger, more angular fragments locally dissected by intragranular fractures (Figures 6d and 6g). The coarser regions (root-mean-squared grain diameter of 2.6 μm for N22) have either equant or moderately elongate morphology, with some 120° triple junctions, although others are closer to 90° (Figures 6e and 7b).

Elongate grains are seen in several fragmented orthopyroxene grains (Figures 6e and 6h, 7, Figure S5 in Supporting Information S1) lying adjacent to the vein margin and have their long axis at a high angle to the vein boundary. Similar elongate fragments also occur adjacent to large intragranular cracks within the orthopyroxene host grain (Figure 6h). Fragmented orthopyroxene occurs also adjacent to non-fractured clinopyroxene, as shown in Figure S5c in Supporting Information S1, where orthopyroxene lamellae within clinopyroxene are fragmented next to the vein margin.

The GOS of the fine-grained fragmented orthopyroxene is low relative to the parent orthopyroxene grain (Figures 7a; S5d in Supporting Information S1). However, low-angle boundaries and higher GOS values are seen in some of the coarser fragments. The finer grains show dispersion of orientations away from the crystallographic orientations of the parent orthopyroxene grain but otherwise are generally similar to the parent orientation (Figures 7b–7d; S5e and S5f in Supporting Information S1). Misorientation axes are scattered in the fractured grain region (Figure 7e), although some clustering around [001] is present (Figure S5f in Supporting Information S1). The more elongate grains have a different CPO to the parent grain; they are preferentially elongate parallel to [001], and show no prominent cluster of misorientation axes (Figure S5g in Supporting Information S1). In general, the fragmented region shows a near-random distribution of misorientation angles between

Figure 3. Microstructures of clinopyroxene in the host anorthosite; (a) fine-grained clinopyroxene ("CPX," plagioclase = "plag") in anorthosite sampled within a shear-zone bounded block but away from any faults—shows detail of Figure 1c (cross-polarised light); (b) clinopyroxene situated 5 mm from vein edge (position indicated in Figure 2d) showing twinning (cross-polarised image); (c) electron backscatter diffraction phase map of clinopyroxene situated 2 mm from vein edge (position indicated in Figure 2d, "Host CPX 1") showing orthopyroxene lamellae, twin boundaries, and scarce low angle boundaries (white lines) which truncate twining (white arrowheads); (d) grain orientation spread (GOS) map across same host rock clinopyroxene with values <5°, indicating level of internal strain; (e) pole figures for host clinopyroxene 1 as shown in (c) with phase coloring (f) IPF (Z) map of clinopyroxene in the immediate margin of the pseudotachylyte (position indicated on Figure 2d, "Host clinopyroxene 2") showing little change in orientation across the grain; (g) GOS map of same clinopyroxene grain showing little internal strain; (h) pole figures for host clinopyroxene 2 as shown in (f) with IPF (Z) coloring.

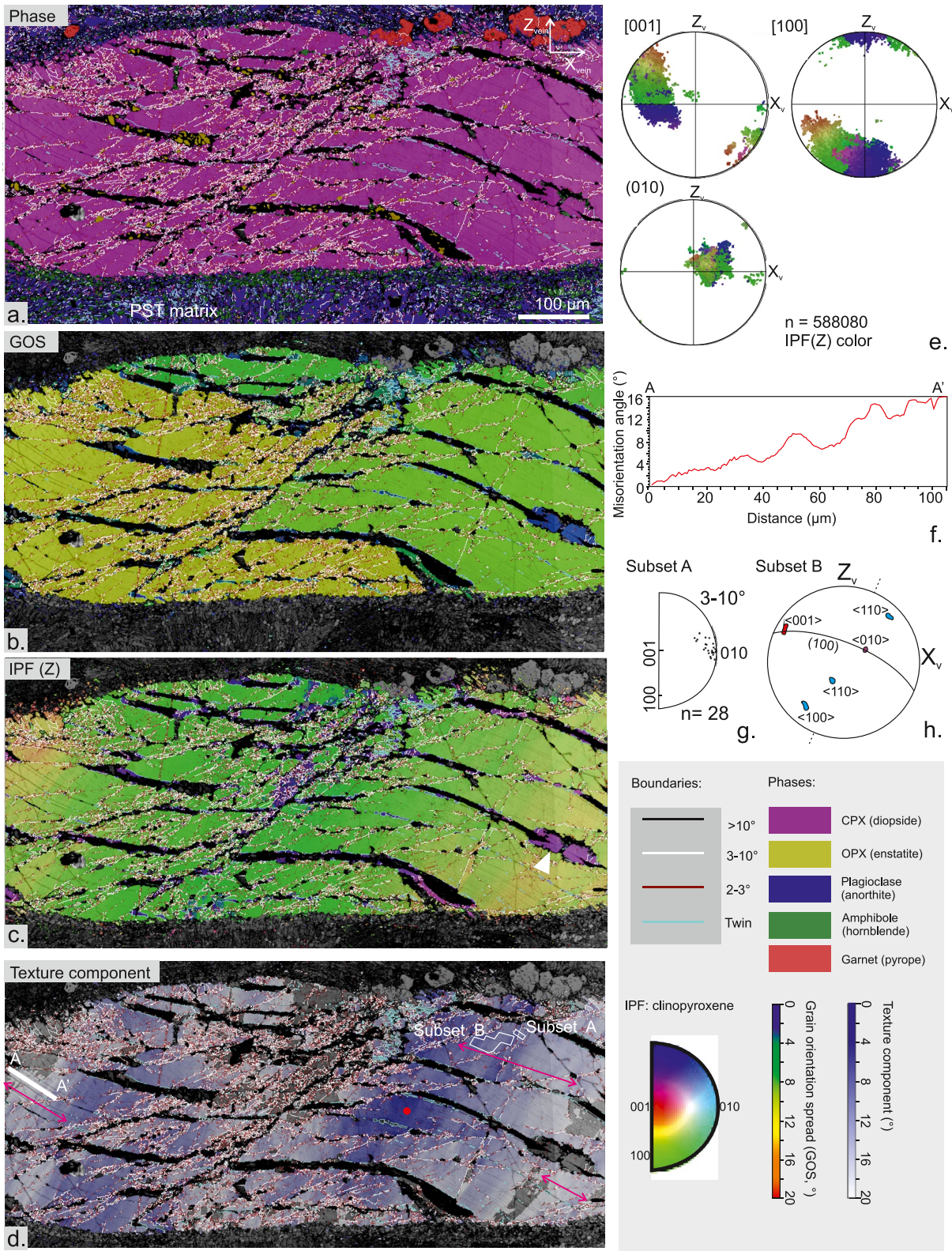
Phase
PST matrix
100 μm
a.
GOS
b.
IPF (Z)
c.
Texture component
Subset B
Subset A
A
A'
d.
[001]
[100]
(010)
n = 588080
IPF(Z) color
e.
Misorientation angle (°)
Distance (μm)
f.
Subset A
Subset B
3-10°
n= 28
g.
h.
Boundaries:
>10°
3-10°
2-3°
Twin
Phases:
CPX (diopside)
OPX (enstatite)
Plagioclase (anorthite)
Amphibole (hornblende)
Garnet (pyrope)
IPF: clinopyroxene
Grain orientation spread (GOS, °)
Texture component (°)

Figure 4.

uncorrelated grains but a higher frequency of misorientations <35° between neighbor grains than for a random distribution (Figures 7f; S5h in Supporting Information S1).

The fractures evident in the BSE images of fragmented orthopyroxene (e.g., Figures 6b, 6c and 6g) correspond either to LABs (i.e., with <10° misorientation across them) or, less frequently, to high-angle boundaries on EBSD maps (Figures 7a–7c). Linear arrays of finer orthopyroxene plus minor clinopyroxene can be seen along the larger of these cracks (Figure 6b), with wider regions of the finer grained material developed in fracture intersections (Figure 6c), but the orientation of the finer-grained orthopyroxene is nearly identical to that of the main grain (Figures 7b and 7c). These linear fractures appear truncated by the zones of more pervasive fracturing (Figures 6d, 7a and 7b).

4.3.2. Grain Size Distribution in the Fragmented Domains

Some of the regions of fragmented orthopyroxene studied for grain-size analysis are shown in Figures 6d–6g (sample N22) and Figures S5a and S5b in Supporting Information S1 (sample LC1724). The sampled set consisted of 2033 grains from N22 and 421 from LC1724. All analyzed images were taken from the fragmented regions of the orthopyroxene grains shown in Figures 6a and 7a. The grain-size distribution curve for both samples shows differences between the smaller and larger grain size ranges (Figure 8). Power law, exponential and log normal lines of best fit were calculated for sections of the distributions. Using the power law exponent, for N22, the slope of the finer grain-size distribution was 2.3 and for the coarser range, 1.2. For LC1724, the finer grained range gave a slope of 1.6, and the coarser range, 3.1 (Figure 8). The break in slope is less pronounced in LC1724; it can best fit by two separate power law trendlines but also by an exponential law. In N22 the break of slope is clear and occurs around 4.7 μm.

4.3.3. Clasts in Pseudotachylytes

Figure 9 shows the EBSD maps of an orthopyroxene clast in the pseudotachylyte matrix of sample LC1724, consisting of microlitic plagioclase and granular clinopyroxene, hornblende and orthopyroxene (Figures 1e and 9a). The clast occurs 3.4 mm from the margin of the PST vein. Undulose extinction and deformation bands are visible optically (Figure 1e). EBSD mapping reveals that these bands represent intracrystalline arrays of fine-grained orthopyroxene with very minor interstitial clinopyroxene and hornblende (Figure 9a). The fine orthopyroxene grains have a maximum GOS of 0.59 (Figure 9b), a maximum D_{equ} of 6.3 μm and a root-mean squared D_{equ} of 2.1 μm. These arrays dissect the host orthopyroxene clast into domains that have accumulated different amounts of internal deformation, as evident from their different GOS values in the 3–8° range (Figure 9b).

The orthopyroxene clast shows slight but repeated undulations with parallel orientation (Figures 9c; S3b in Supporting Information S1). These undulations are locally parallel to sharp, linear, very low-angle boundaries (1–3°, red lines) (Figure 9c). These periodic undulations and the 1–3° low-angle boundaries occur on a semi-regular wavelength of 10–20 μm, giving a crenulated undulose effect (Figure 9d). The misorientation axis associated with these bands is [001] (Figure 9e), which is consistent with slip on the (100) [010] system assuming a tilt boundary geometry. The undulations and the low-angle boundaries are cut by the arrays of fine-grained orthopyroxene.

The fine-grained orthopyroxene share a CPO with the host clast, although some dispersion is present (Figure 9f). The dispersion predominantly occurs around [001]. Polygonal networks of low-angle boundaries, potentially indicating the development of subgrains, have not been observed in the clast.

Figure 4. Microstructure of clinopyroxene clast "1" from electron backscatter diffraction analysis (position shown in Figure 2d); (a) Phase map highlighting bent orthopyroxene lamellae, twin boundaries and low angle boundaries (white lines, 3–10°); (b) grain orientation spread map illustrating variable, but moderate, internal strain across the clinopyroxene grain. Twin lamellae have very low (blue) values; (c) IPF (Z) orientation map of clinopyroxene. Lattice distortion of the entire grain is clear, as are twinned regions (showing in purple) A sudden widening of a twin lamellae is show by white arrowhead; (d) texture component map (for clinopyroxene only) showing degrees of misorientation away from the reference point (red circle). Smaller-wavelength undulations are most easily seen here, strongly developed over regions indicated by pink arrows; (e) pole figures (lower hemisphere) for [001] and [100] axes and poles to (010) planes of clast 1; (f) misorientation profile from A-A' (location indicated in d.) showing regular 20–40 μm undulation of the lattice. The progressive increase in misorientation from point A is due to the long wavelength kinking of the clast; (g) Rotation axes shown in crystal co-ordinates and crystal axes shown in sample co-ordinates for subset A, indicated in (d)); (h) pole figures for undulating region "subset B" (indicated in d.), used for boundary trace analysis. The rotation axis [010] is indicated in purple and the suggested slip direction in red. The boundary trace parallel to the periodic undulation is indicated by the dashed lines.

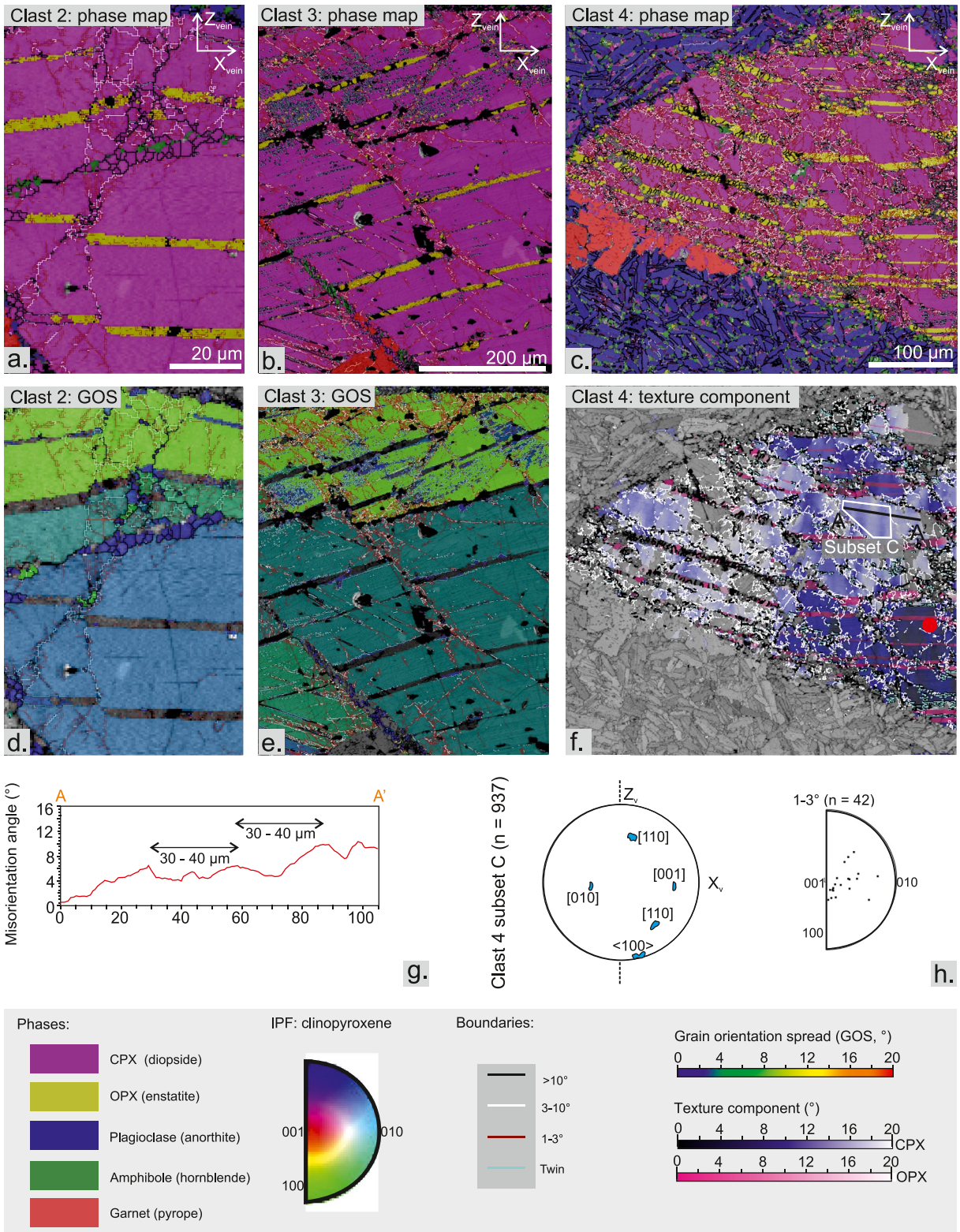
Clast 2: phase map
Clast 3: phase map
Clast 4: phase map
20 μm
200 μm
100 μm
a.
b.
c.
Clast 2: GOS
Clast 3: GOS
Clast 4: texture component
Subset C
d.
e.
f.
Misorientation angle (°)
A
A'
30 - 40 μm
30 - 40 μm
g.
Clast 4 subset C (n = 937)
[110]
[001]
[010]
[110]
<100>
1-3° (n = 42)
001
010
100
h.
Phases:
CPX (diopside)
OPX (enstatite)
Plagioclase (anorthite)
Amphibole (hornblende)
Garnet (pyrope)
IPF: clinopyroxene
Boundaries:
>10°
3-10°
1-3°
Twin
Grain orientation spread (GOS, °)
Texture component (°)
CPX
OPX

Figure 5.

5. Discussion

5.1. Overprinting Relationships Between Deformation Microstructures

Twins occur in clinopyroxene, both within clasts in the pseudotachylyte veins—interpreted to be survivor clasts that did not break down during coseismic melting - and in host rock grains situated at least up to 8 mm away from the vein margin (Figure 3b). Twins in the host rock appear more frequently developed on (001), whereas clasts record a mixture of (100) and some (001). In clasts 1 (Figure 4) and 3 (Figure 5b), the clustering of discontinuous twins near the clast boundary implies that at least some twinning may have been driven by localized deformation conditions in the slipping fault zone. Twin boundaries are generally bent and cut by other microstructures, including LABs, cracks, and periodic low (1–3°) misorientation bands (Figures 4 and 5), implying that twins are typically the earliest microstructure recorded within clinopyroxene (Table 1), and extends some distance into the wall-rock.

Other deformation microstructures are limited to clasts within the pseudotachylyte fault vein, suggesting that they relate to highly localized deformation associated with the earthquake rupture. These include the periodic undulations with 20–40 μm wavelength, which overprint orthopyroxene exsolution lamellae (Figure 5f) and deformation twins, but are themselves cut and offset by fracturing (Figure 4) and sometimes by grain growth in intracrystalline bands of fine-grained clinopyroxene ± amphibole ± garnet (Figures 5a and 5b).

In orthopyroxene (Table 1), fracturing and fragmentation are preserved in grains in the wall rock margin as well as in survivor clasts. In the wall-rock margin, the dominant microstructure is spaced fracturing (Figures 6b and 6c) with local regions of pervasive fragmentation (Figures 6 and 7; S5 in Supporting Information S1). In the orthopyroxene clast analyzed with EBSD, undulating misorientation resulting from glide on (100) [010] is cut by intracrystalline bands of fine-grained orthopyroxene ± clinopyroxene ± amphibole (Figure 9). Because other orthopyroxene clasts show pervasive fragmentation similar to the margin grains (Figure S6 in Supporting Information S1), we suggest that the analyzed orthopyroxene clast in Figure 8 preserves the earlier signature of dislocation glide, which has escaped fragmentation.

In summary, we interpret these overprinting relationships (Table 1) to reflect the prerupture to coseismic deformation of pyroxene in response to local stress amplifications that triggered the generation of type-2 pseudotachylytes in Nusfjord. In the following sections, we propose a conceptual model associating these stress changes with the seismic cycle already partly recorded by the presence of pseudotachylyte.

5.2. High-Stress Loading: Deformation by Low-Temperature Plasticity

We identify thin (<10 μm wide) repeated lamellar twins in the clinopyroxene clasts (Figures 4 and 5) as mechanical (deformation) twinning (Raleigh & Talbot, 1967), an idea supported by some clustering in regions of the clast which may have experienced stress concentrations (Figure 5e). Some wider twins in clast 1 (Fig. 4c—purple regions on IPF map) are potentially more characteristic of growth twins; the rapid thickening of the prominent twin on the far right is similar to the "bursting" of growth twins that have been modified by mechanical twinning (Kollé & Blacic, 1982). However, we have not observed the associated microtwins that occur in the clinopyroxene example of Kollé and Blacic (1982). Between these thicker twins, fine-lamellar twins are more prevalent than mapped by EBSD analysis, with additional lamellae that we interpret to be mechanical twins visible in the underlying band contrast image (best seen in the lower right corner of Figure 4d). (100) is usually noted as the prominent mechanical twin plane in clinopyroxene (Avé Lallemant, 1978; Kollé & Blacic, 1982), although (001) can also host deformation twins (Raleigh & Talbot, 1967). In our host-rock grains, (001) is mostly seen forming the twin plane. However, the twin width is similar to that observed in the clasts and also form multiple parallel lamellae, so we also consider these to be predominantly mechanical twins. Overall, all of the twinned clinopyroxenes analyzed here are interpreted to display some mechanically derived twins.

Figure 5. Microstructures of clinopyroxene clasts 2–4 from electron backscatter diffraction analysis (positions shown in Figures 2d and 2f); (a) phase map of part of clast two; (b) phase map of part of clast 3; (c) phase map of part of clast 4; plus the surrounding pseudotachylyte matrix; (d) grain orientation spread (GOS) map of clast 2 (clinopyroxene only) showing increasing values toward the clast edge (top), and very low values in the fine grained crack fill; (e) GOS map of clast 3 (clinopyroxene only) showing increasing values toward the clast edge, and very low values in clinopyroxene twins and in fine grained crack fill; (f) texture component map for clast 4 showing misorientation relative to the reference point (red dot). Clinopyroxene is mapped in blue and orthopyroxene in pink; (g) misorientation profiles for A-A' (shown in f.) highlighting regular undulations; (h) orientation of axes in clinopyroxene clast 4 (location of subset c shown in f.). The boundary trace parallel to the periodic undulation is indicated by the dashed lines. Rotation axes are displayed in crystal co-ordinates for the same subset.

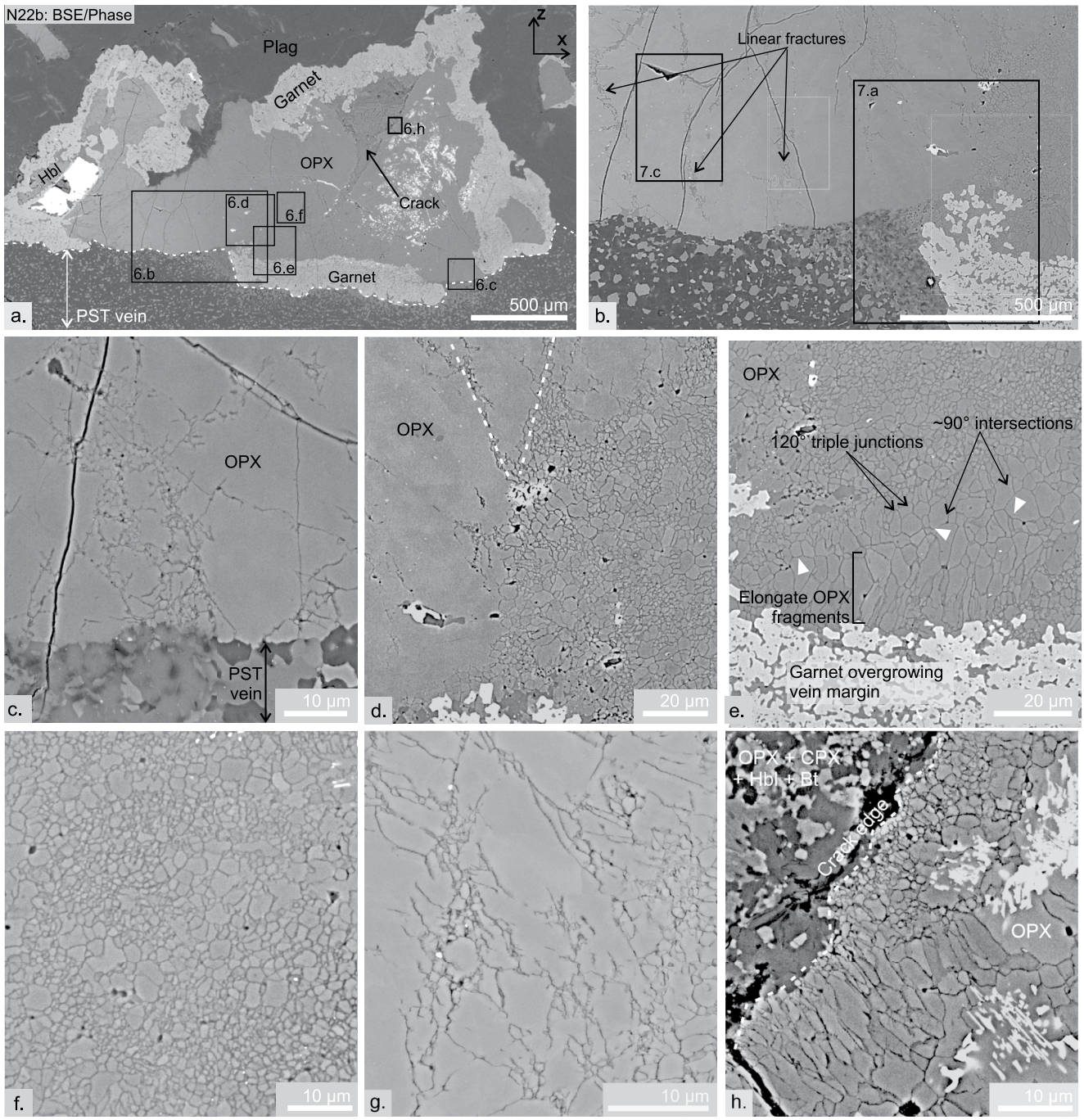

Figure 6. Backscattered electron images of orthopyroxene grain and adjacent pseudotachylyte vein in sample N22: (a) View of orthopyroxene grain on margin of pseudotachylyte vein with adjoining phases and subsequent image locations labeled; (b) Higher magnification view of same grain illustrating fracture sets across left hand side of grain. Map locations for electron backscatter diffraction analysis shown in Figure 7 are indicated; (c) jigsaw-like fragmentation along cracks; (d) edge of pervasively fragmented region. Dashed white lines indicate the main fracture orientations where they meet the fragmented region; (e) Variation in fragment size and morphology in pervasively fragmented region. Some triple junctions show 120° angles and others show some curvature to intersect nearer to 90°. White arrowheads indicate coarse grain concave faces in contact with smaller grains; (f) high-magnification image of pervasively fragmented region, showing finest grains; (g) edge of fragmented region with coarse fragments; (h) fragmentation of orthopyroxene around an internal crack filled with biotite plus minor orthopyroxene, clinopyroxene and hornblende.

Deformation twinning via (100)[001] in diopside occurs at a critically resolved shear stress of 100–140 MPa but is not dependent on temperature or strain rate and is produced by dislocation glide (Kollé & Blacic, 1982). Similar values were derived for jadeite (150 ± 25 MPa) by Orzol et al. (2003). Twinning in host-rock clinopyroxene

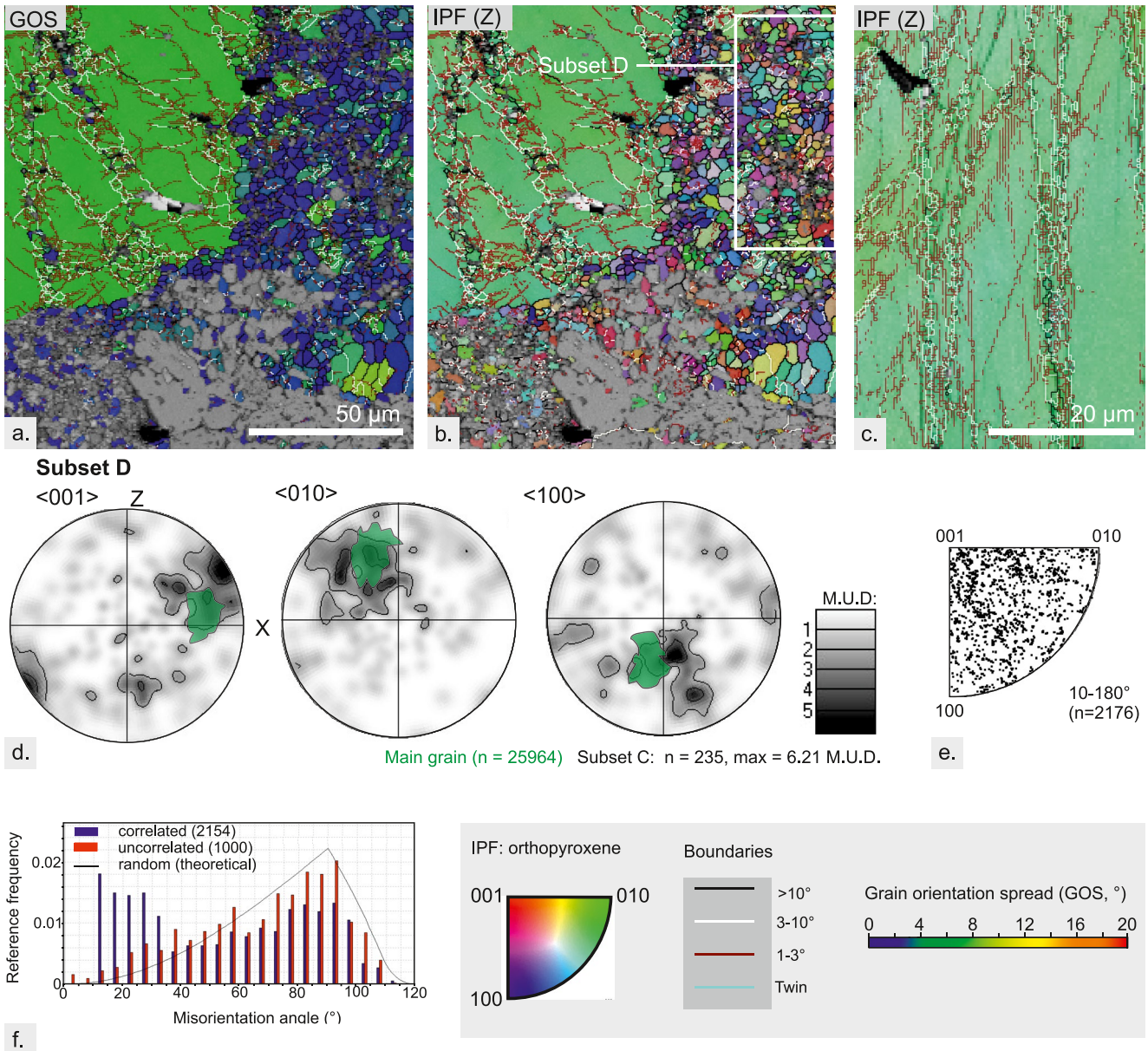

Figure 7. Microstructures of orthopyroxene in the host rock margin to a pseudotachylyte vein from electron backscatter diffraction analysis (map positions shown in Figure 6): (a) grain orientation spread map of edge of fragmented orthopyroxene (b) IPF (Z) orientation map of orthopyroxene in same region as (a); (c) IPF (Z) orientation map of region in center of orthopyroxene grain (d) pole figures for sample of fragmented region—location of this subset D shown (b); (e) rotation axes (in crystal co-ordinates) pole figures for subset (d); (f) misorientation angle histogram for subset (d).

grains away from the vein margin suggests that this early stage of deformation was driven by stresses that were not entirely localized along the future fault zone. This may be related to the earliest heterogeneous stress amplification that built up prior to any individual brittle failure, less localized to the eventual rupture zone than the later clast microstructures that all cross-cut twins. The change in twin law between the host-rock grains (001) [100] and the clasts (100) [001] is likely to be coincidental but driven by the orientation of the principal stresses (Kollé & Blacic, 1982; Trepmann & Stöckhert, 2001). In the case that the twinning was driven in variously orientated crystals by a single loading event, the differential stress can be assumed to be significantly higher than double the critically resolved shear stress (Küster & Stöckhert, 1999). However, similarly to the interpretations of Trepmann and Stöckhert (2001) on naturally deformed, mechanically twinned jadeite, the relatively spatially prevalent twins could be produced by multiple cycles of loading across the anorthosite block. In our framework this equates to cyclical prerupture stress amplification, although not all cycles may have always achieved the critical brittle

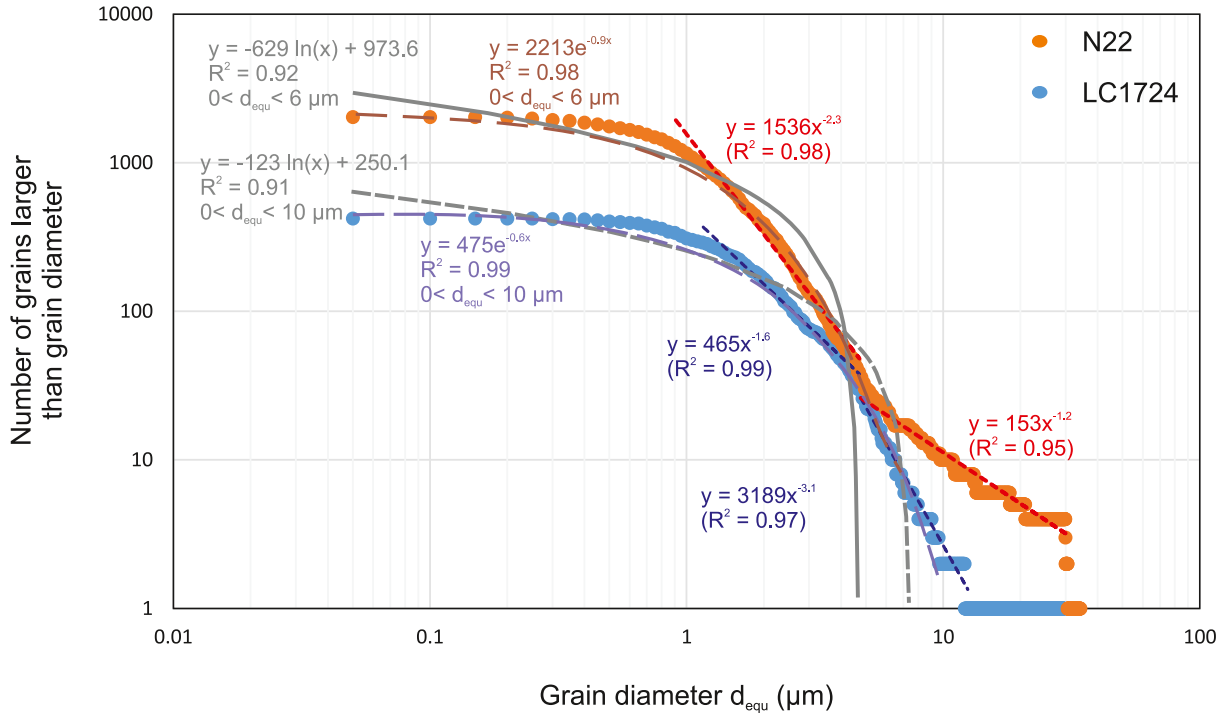

Figure 8. Grain size distribution for fragmented orthopyroxene in vein margins for samples N22 and LC1724. Best fit lines are shown for log normal (gray), power law (red/blue), and exponential (purple/brown) distributions.

failure stress. Twinning in naturally deformed clinopyroxenes has been interpreted elsewhere as a feasible strain response to instantaneous stress changes in the context of deformation conditions at shallower crustal levels (Orzol et al., 2003; Trepmann & Stöckhert, 2001), but such instantaneous stress changes are not a necessity for twinning and are not required for the lower crustal setting of Nusfjord.

Most clinopyroxene clasts illustrated here show further deformation by low-temperature plasticity controlled by dislocation glide along (100) [001], producing undulating misorientations that cut the twin boundaries and the orthopyroxene exsolution lamellae. (100) [001] is the typical glide system in clinopyroxene (Avé Lallemant, 1978; Ingrin et al., 1992; Kirby & Kronenberg, 1984; Kollé & Blacic, 1983; Raleigh & Talbot, 1967). In our samples, evidence of any transition to dislocation climb is absent, consistent with the relatively low temperature conditions of deformation for crystal plasticity in clinopyroxene (e.g., Bystricky & Mackwell, 2001). Flow laws extrapolated to natural strain rates for dislocation glide of diopside require several 100 MPa or GPa of differential stress for Peierls-controlled glide to occur in clinopyroxene (Figure 10, Table S1 in Supporting Information S1). The micro-indentation tests of Dorner and Stöckhert (2004) suggest that, even relatively low strain rates of 10^{-14} s^{-1} at deformation temperatures of 600–700°C require flow stresses >1 GPa in order to activate Peierls-controlled glide. If strain rates were to increase toward seismic strain rates, the required flow stress would increase further (Figure 10). Based on the flow law for Peierls-controlled glide of Kollé and Blacic (1983), at temperatures of 600–700°C, strain rates >10^{-12} s^{-1} are necessary to induce glide, and at strain rates of 10^{-9} s^{-1} or greater, critical resolved shear stresses would be >1 GPa (at 700°C) and >3 GPa (at 600°C) (Figure 10). This glide law was observed by Kollé and Blacic (1983) to initiate at critically resolved shear stresses >520 MPa in hedenbergite crystals poorly orientated for twinning; in crystals where twinning was possible, dislocation glide required temperatures >850°C under their experimental conditions. Without knowing the stress orientation, the calculation of an equivalent absolute differential stress is not possible but the differential stress must be at least twice the resolved shear stress. We therefore infer that the low-temperature plasticity microstructures observed in clinopyroxene clasts occurred as a response to transient and localized differential stresses in excess of 1 GPa. The localization of these microstructures to the clasts, being absent in the clinopyroxene grains which now form the margin to the pseudotachylyte vein, suggests that these high stresses were localized to the rock volume that subsequently formed the pseudotachylyte fault vein. However, overprinting by fracturing and fragmentation indicates that this

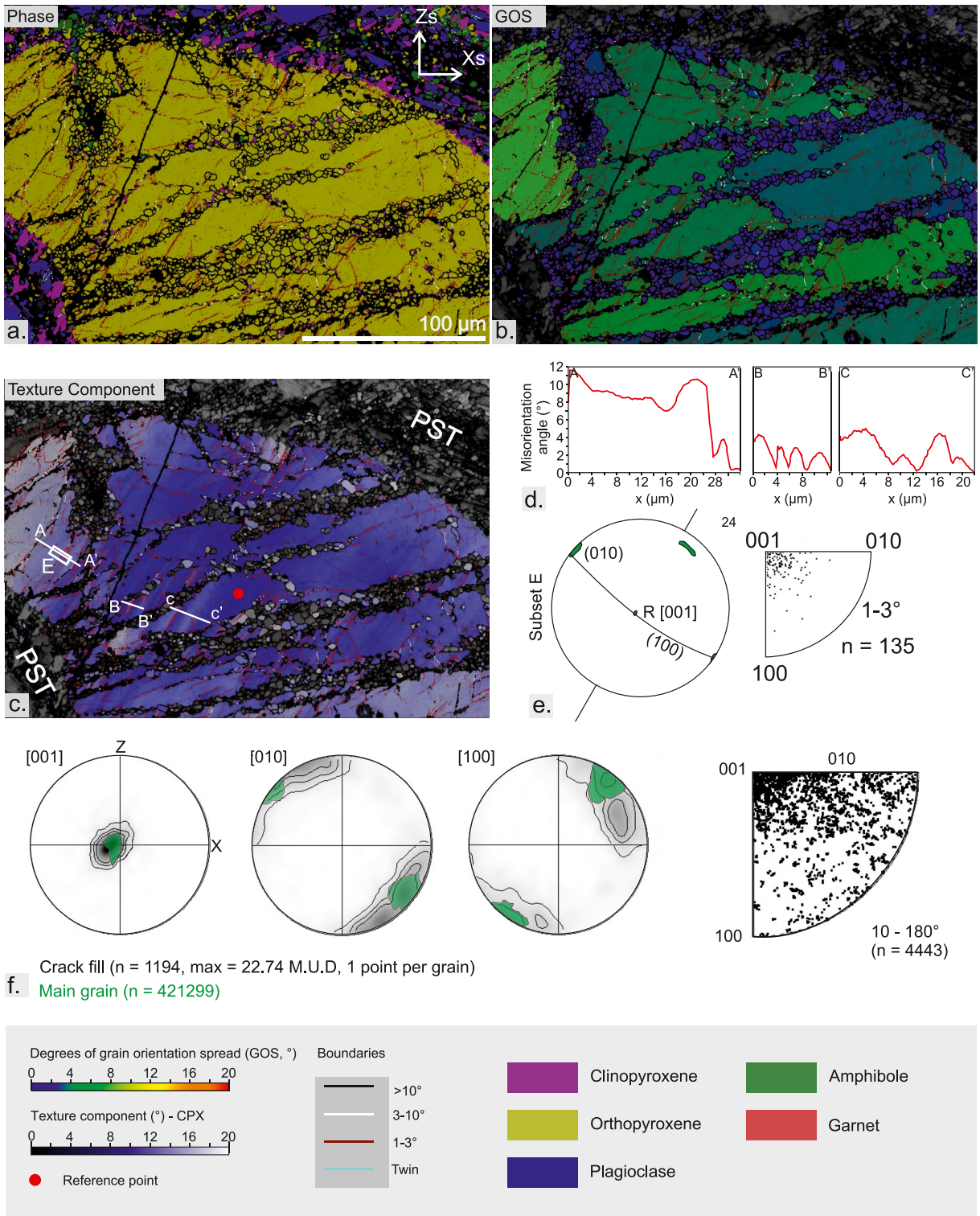

Figure 9. Microstructures of orthopyroxene clast from electron backscatter diffraction analysis; (a) Phase map of analyzed region of clast and surrounding pseudotachylyte matrix; (b) grain orientation spread (GOS) map of orthopyroxene. Fine-grained arrays of orthopyroxene have low GOS values (blue coloring); (c) Texture component map of orthopyroxene, red dot locates reference point; (d) misorientation profiles along A-A' B-B' and C-C', indicated in (c); (e) pole figure and low-angle rotation axes (in crystal co-ordinates) for subset D, location shown in (c); (f) pole figures and high-angle rotation axes for the fine-grained orthopyroxene arrays within the clast. Green overlay shows distribution of points from the main grain.

Table 1
Overprinting Order of Microstructures Seen in Clasts and Host-Rock Pyroxenes (No Equivalence in Time Is Implied Across Clinopyroxene and Orthopyroxene Microstructures Here)

	Clinopyroxene	Orthopyroxene
Earliest	Twinning (low T plasticity)—host rock and clasts	Periodic undulations (low T plasticity) - clasts
	Periodic undulations (low T plasticity)–clasts	Fractures, fragmented regions—host rock and clasts
	Fractures–clasts	Triple junctions in monophase fine-grained assemblages, appearance of polyphase fine-grained assemblage—host rock and clasts
Latest	Fine-grained mixed phase assemblages–clasts	

high-stress deformation occurred prior to the passage of the rupture tip. This could occur during prerupture loading, or coseismically, as part of the process zone deformation.

The regular 20–40 μm wavelength periodic undulation of the clinopyroxene lattice (Figures 4f and 5g) bears some similarities to the short-wavelength undulatory extinction (SWUE) recognized in quartz (Trepmann & Stöckhert, 2013) and olivine (Druiventak et al., 2012) "kick-and-cook" experiments. However, the undulation seen here in clinopyroxene has a longer wavelength. The undulose misorientation is characterized purely by continuous sinusoidal curvature of the crystal lattice, which was accommodated by glide along the (100)[001]. Similar periodic undulations also occur in orthopyroxene clasts (Figure 9d) and are consistent with dislocation glide on (100)[010] (Figure 9e).

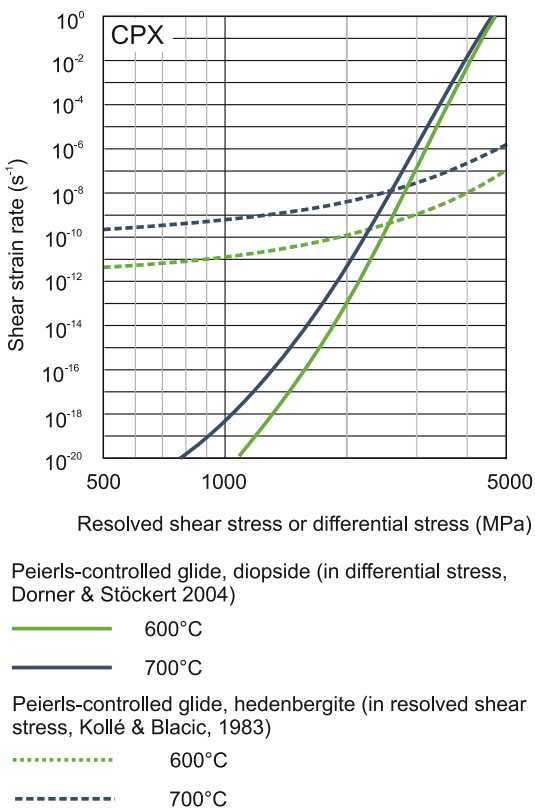

Figure 10. Two flow laws for Peierls-controlled glide in diopside (Dorner & Stöckhert, 2004) and hedenbergite (Kollé & Blacic, 1983) at temperatures for deformation in Nusfjord (600–700°C). The law from Dorner and Stöckhert (2004) is relevant for a temperature range of 350–750°C and uses their "model I" value for pre-exponential factor. The law from Kollé and Blacic (1983) is for Peierls glide on (100) [001] for <900°C and >520 MPa. Note that the x-axis shows differential stress for Dorner and Stöckhert (2004) but resolved shear stress for the laws of Kollé and Blacic (1983).

The formation of SWUE in quartz was attributed to high-stress dislocation glide ("kick"-phase) that generates lamellae of tangled dislocations (Trepmann & Stöckhert, 2013). Natural comparisons to SWUEs have been proposed in quartz (Birtel & Stöckhert, 2008; Brückner & Trepmann, 2021; Trepmann & Seybold, 2019) and olivine (Matysiak & Trepmann, 2012) but not previously, to our knowledge, in pyroxenes. The generation model for SWUEs of Trepmann and Stöckhert (2013), invoking dislocation glide under high stresses caused by seismic loading, is inviting because of the shared deformation mechanism (glide) observed in these pyroxenes, and because of the earthquake context of the Nusfjord samples. The parallels are especially clear in the recent work of Brückner and Trepmann (2021) who observe SWUEs in quartz adjacent to pseudotachylytes. We propose that the periodic undulations in clinopyroxene were produced by a low-temperature plasticity response to the highest stresses localized around the eventual fault plane in the prerupture loading phase. After twinning, the periodic undulations are the next earliest microstructure to form in clinopyroxene, and in orthopyroxene are cut by fractures. Hence they are potentially related to the stress concentrations during loading, preceding eventual rupture. These stress concentrations are consistent, also in their magnitude, with the interpretation that prerupture stress amplification within the anorthosite blocks was driven and governed by geometrical effects of viscous creep activity along the coeval bounding shear zones (Campbell et al., 2020).

SWUEs in quartz and olivine were attributed to high-stress loading of the mid-to lower-crust via shallower earthquake activity (Birtel & Stöckhert, 2008; Matysiak & Trepmann, 2012; Trepmann & Stöckhert, 2013). The context of the seismic environment in Nusfjord, where type-2 pseudotachylytes represent the in situ nucleation of short earthquake ruptures (Campbell et al., 2020), fits better with the observations of Brückner and Trepmann (2021) that such glide-controlled microstructures also occur adjacent to in situ earthquake rupture within the mid-to lower-crust. Our evidence supports transient high-stress loading either being a result of local stress

amplification preceding and eventually causing rupture nucleation (Campbell et al., 2020), to the process zone preceding the rupture tip, and/or as a response to high rupture-tip stresses (Reches & Dewers, 2005). The former is preferred due to the overprinting of glide structures in orthopyroxene by later fragmentation that can be linked with more confidence to dynamic rupture-tip processes.

5.3. Coseismic Deformation: Pulverization of Orthopyroxene

The fine-grained orthopyroxene at the pseudotachylyte fault vein margin (Figures 6 and 7) is interpreted to have formed via brittle grain size reduction, based on: (a) the fracture systems evident in BSE micrographs (Figure 6) and the jigsaw-breccia type grain shapes preserved in some fine-grained regions (Figure 6g), and (b) the absence of polygonal subgrains from the interior of the large orthopyroxene fragments, in accordance with the expected lack of recovery in orthopyroxene at the deformation temperature of 700–750°C (e.g., Kanagawa et al., 2008; Kohlstedt & Vander Sande, 1973). This jigsaw-style geometry, preservation of the overall shape of the parent crystal (Johnson et al., 2021), and general lack of evidence for cataclastic processes such as grinding, fragment rotation and frictional slip, are also indicative of a lack of shear displacement (Figure 7d, see also Petley-Ragan et al., 2019; Soda & Okudaira, 2018; B. R. Song et al., 2020). Together, these observations support a mostly tensile origin for this fragmentation within the orthopyroxene. We use the descriptive term "pulverization-style fragmentation" to describe the observed fragmentation, which is pervasive over an area of >50 μm but may be contained within only one or two parent grains. It should be noted that in comparison to recent robust definitions of pulverization on a field scale, these microstructures would be considered highly selective and could be categorized as "selective, non-pervasive pulverization" (based on fragment size) or "selective, non-pervasive microstructural shattering" (based on microstructural style) under the recent classification of Ostermeijer et al. (2022).

An alternative explanation for fragmentation driven by thermal shock was ruled out due to the lack of fracturing in the orthopyroxene clast (Figure 9), which, being within the vein, should have experienced higher coseismic temperatures than the wall rock (Papa et al., 2018). However, other orthopyroxene clasts do show pervasive fragmentation for which thermal shock cannot be ruled out (Figure S6 in Supporting Information S1). It is possible that thermal shock fragmentation did indeed take place across many phases, localized to the outer clast edges that experienced the most rapid temperature change, and that the fragmented regions were preferentially removed during the coseismic slip phase by disaggregation and/or partial melting favoring small grain sizes (Papa et al., 2018). However, we do not see enough evidence that favors thermal shock as a driver of fragmentation within host-rock orthopyroxenes.

Although pulverization is considered to be depth-limited by increasing confining pressure (Aben et al., 2017; Yuan et al., 2011), pervasive damage zones extending up to 200 m from the fault have been exhumed from crustal depths around the frictional viscous transition (Sullivan & Peterman, 2017; B. R. Song et al., 2020; W. J. Song et al., 2020; Johnson et al., 2021). Interpretations of pulverization of single grains have recently accumulated from microstructural studies of lower crustal earthquakes in both naturally and experimentally deformed rocks (Austrheim et al., 2017; Incel et al., 2019; Petley-Ragan et al., 2019; B. R. Song et al., 2020; Soda & Okudaira, 2018). Minerals observed to undergo pulverization-style fragmentation include plagioclase (Pittarello et al., 2008; Soda & Okudaira, 2018; B. R. Song et al., 2020), garnet (Austrheim et al., 2017; Incel et al., 2019; Manktelow et al., 2022; Petley-Ragan et al., 2019; B. R. Song et al., 2020) and diopside (Petley-Ragan et al., 2019). In the Nusfjord samples, orthopyroxene is the only mineral to show microstructures compatible with pulverization style fragmentation, although on a centimeter-scale the wider anorthosite is intensely fractured in places.

Pulverization-style fragmentation, particularly where tensile fracturing is involved, is attributed to dynamic rupture-tip stress fields that overcome the high confining pressure (Reches & Dewers, 2005), but has also been linked to impulsive coseismic loading and unloading of the wall-rocks (Brune, 2001), or to the passage of high-energy stress waves ahead of the rupture front or around rough fault geometries, which can explain fragmentation at greater distances from the slip plane (Doan & Gary, 2009; Johnson et al., 2021 and references therein). The asymmetry of fragmentation observed in the field along major tectonic faults favor a link with the asymmetric rupture-tip stress fields, where one side of the tip is in compression and the other in tension (Dor et al., 2006; Petley-Ragan et al., 2019; Reches & Dewers, 2005; Wilson et al., 2005; Xu & Ben-Zion, 2017). Although supershear ruptures may favor pulverization (Yuan et al., 2011), sub-shear ruptures should also induce extreme stress and strain rate conditions a few mm from the rupture—one calculation predicts 5 GPa tensional stress and $\sim 10^5\ s^{-1}$ dilation in this zone (Wilson et al., 2005). In our samples, it is not easy to judge whether the

pulverization style fragmentation occurs on one side of the fault only, because there is no orthopyroxene visible in the opposing wall to compare with. While fragmented orthopyroxene occurs within clasts in the vein, the delocalization effect of the pseudotachylyte melt makes it impossible to know where the initial rupture plane was in relation to the in situ position of that grain. There is evidence for injection veins and damage on both sides of the fault in one sample (Figures 2c and 2d), which may dispute asymmetry (although injection veins are not always linked to rupture-tip stress fields). However, the alternative models of impulsive loading cycles or high-energy stress waves (Brune, 2001; Doan & Gary, 2009) are also coseismic processes and as such this uncertainty does not change our interpretation of the timing of these microstructures.

5.4. Grain Growth of Orthopyroxene Driven by a Short-Term Heat Pulse

Many of the orthopyroxene fragmented grains are somewhat modified in shape. Grain growth from the fine-grained fragments is apparent in the elongate orthopyroxene grains and in regions with well-developed 120° triple junctions (Figure 6e), which along with concave faces of larger grains suggest a greater influence of surface-energy over strain-energy driven grain boundary migration (Platt & Behr, 2011), although a mix of concavo-convex boundary forms can be seen (Figure 6e). Grain-size distributions (Figure 8) are commonly used to determine processes of fracturing, faulting, and grain growth (e.g., Aupart et al., 2018; Keulen et al., 2007; Muto et al., 2015), although distinguishing mechanisms of brittle fragmentation is not always certain based on this analysis alone (Stünitz et al., 2010; Wilson et al., 2005). The observed range of 2D power law slope values in our analysis, 1.2–3.1 (Figure 8), is comparable with grain-size distributions reported for mid-to lower-crustal earthquake damage (Aupart et al., 2018 and references therein; Jamtveit et al., 2019; Soda & Okudaira, 2018; B. R. Song et al., 2020) including those attributed to coseismic pulverization of garnet, olivine, and plagioclase. Neither of our samples are conducive to a single best-fit power law or log normal distribution, with the break in slope estimated at a diameter of around 4.7 μm for both samples, but LC1724 can also be fitted relatively satisfactorily with an exponential law (Figure 8). A calculation of the grinding limit for pyroxene (jadeite, in the absence of fracture toughness data for enstatite) using the crack nucleation model of Hagan (1981), which approximates the threshold crack size as $c \approx 30(K_{IC}/H)^2$ (where H is hardness ($H_{jadeite} = \sim 5$, Spray, 2010) and K_{IC} is the fracture toughness ($K_{ICjadeite} = 0.7$ MPa m^{-2}, Spray, 2010), gives a threshold crack size of 0.4 μm. Despite uncertainties in the parameters, this is significantly smaller than the grain size (~ crack size) at the break of slope (Figure 8), which is therefore unlikely to be related to the grinding limit. A two-stage fracturing process has been suggested for bifractal distributions elsewhere (B. R. Song et al., 2020) involving an initial high strain rate coarse fragmentation modified by a finer fragmentation focused along the initial fractures, representative of some frictional sliding. However, we do not observe the clusters and arrays of finer fragments along larger cracks and their intersections (Figure 6d), which B.R. Song et al. (2020) use to support this (their figure 7). Another source of multi-stage fracturing would be multiple deformation events with mixes of dynamic loadings at differing strain rates (Aben et al., 2016), but there is no evidence in these samples that the faults have undergone multiple slip phases (Campbell et al., 2020). Instead we suggest that this change in slope, if physically present, could reflect modification of the original fragmentation grain size by the subsequent grain growth apparent in the BSE images. This is consistent with the findings of Keulen et al. (2007) and Aupart et al. (2018) that changes in GSD slope reflect a switch in grain processes, although it should be noted that those studies looked at shear deformation rather than tensile fragmentation.

The CPO of the elongate grains differs from that of the more equant fragments, which tend to be similar to the parent CPO (Figures S5f and S5g in Supporting Information S1). The short axes of the elongate grains are of a similar size to the diameter of the equant grains, and angular triple junctions are developed between adjacent fragments (Figures 6e and 6h) suggesting that the elongate grains may have formed via growth of the initial fragments, possibly with some component of rotation. The shape preferred orientation is always at a high angle to the vein edge (Figures 6 and 7, Figure S5 in Supporting Information S1) and the grain elongation is predominantly parallel to [001], which has been reported as the fastest diffusion and growth direction in orthopyroxene (Dohmen et al., 2016; Milke et al., 2013). This elongation is also observed at the edge of a large intracrystalline tensile crack within a host-rock-margin orthopyroxene grain (Figures 6a and 6h) which extends between points of 0.34–1.09 mm perpendicular distance from the pseudotachylyte vein edge. The apparent orientation of the crack forms a high angle to the fault vein, suggesting that the crack was tensile, as does the parallel elongation of the orthopyroxene perpendicular to the crack. This geometry is similar to tensile cracks formed within dynamic stress fields linked to crack tip propagation (Ngo et al., 2012), suggesting that it may have formed concurrently

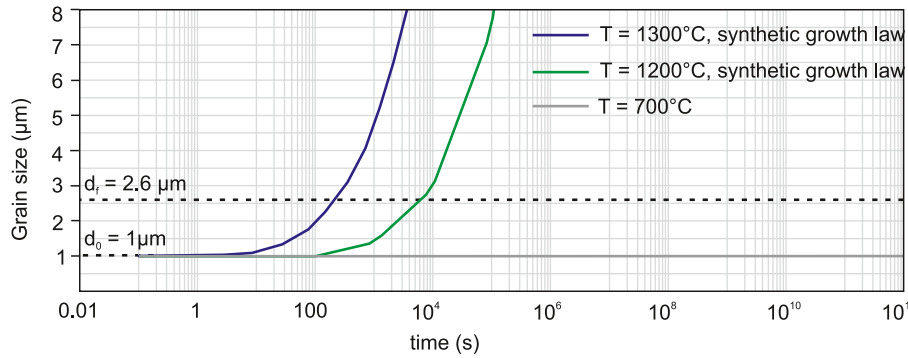

Figure 11. OPX grain growth modeling from initial diameter of 1 µm. Growth law parameters from the synthetic samples of Skemer and Karato (2007) are used to compare rates for 1300°C and 1200°C; for 700°C, the rate constant k (rate constant) is extrapolated from enthalpy and k_0 values provided in the same publication.

with the pulverization style fragmentation within the grain. The distribution of the elongate grains along the edge of this crack and along the pseudotachylyte vein margin therefore implies that elongate grain growth occurred after fragmentation but potentially concurrently with continued slip and the associated frictionally generated thermal pulse that drove melting along the fault plane. No significant compositional changes have been identified via energy dispersive X-ray spectroscopy analysis across fragments suspected to have undergone growth, but the small fragment size makes resolving such changes difficult.

Because of the transience of frictional heating, grain growth needs to take place during or immediately after earthquake slip. Using the orthopyroxene grain growth laws of Skemer and Karato (2007), we assess the potential growth time necessary for a starting orthopyroxene fragment size of 1.0 µm at temperatures ranging from 1300°C - close to typical pseudotachylyte maximum melt temperatures (Sibson & Toy, 2006) - down to an ambient temperature of 700°C (Figure 11). At 700°C, the orthopyroxene will not achieve the required grain size of D_{equ} = 2.6 µm (for the elongate grains) within 3 Gyr, implying that some form of a heat pulse must be required for grain growth. At temperatures around 1300°C, the required grain growth may be achieved within 16 min and at 1200°C, within 3 hr (Figure 11). These temperatures can be feasibly generated during coseismic frictional heating, so that growth of the elongate grains likely initiated during slip.

5.5. Conceptual Model of Prerupture and Coseismic Deformation in Pyroxenes

Based on the overprinting relationships of microstructures in the pyroxenes (Table 1) and our interpretations of their deformation mechanisms plus resulting stress and temperature implications, we suggest a conceptual model of prerupture and coseismic deformation of clinopyroxene and orthopyroxene (Figure 12).

1. Distributed twins seen in clinopyroxene appear to be spatially associated with pseudotachylyte veins but are not as localized as subsequent deformation microstructures. The critical shear stresses associated with clinopyroxene twinning (Kollé & Blacic, 1982; Orzol et al., 2003), although significant (100s MPa), are not necessarily high relative to expected brittle failure strength (GPa); twinning may relate to progressive stress amplification prior to the brittle failure stress being reached (Campbell et al., 2020), driving the onset of dislocation glide.
2. Low-temperature plasticity other than twinning in clinopyroxene and orthopyroxene is predominantly found within clasts, suggesting a much more pronounced localization of stress (potentially >1 GPa, Figure 10) around the eventual rupture plane. This interpretation is consistent with those made for similar high-stress dislocation-glide-controlled microstructures observed in naturally and experimentally deformed rocks (Druiventak et al., 2011; Matysiak & Trepmann, 2012; Trepmann et al., 2013).
3. Low-temperature plasticity is overprinted by pulverization style fragmentation in orthopyroxene, which most likely relates to dynamic stress fields associated with the passage of the rupture tip (the "fault tip process zone" of Petley-Ragan et al., 2018—their figure 4), or may relate to impulsive loading or high energy stress waves. There appears to be no microstructural record for this stage in the clinopyroxene.

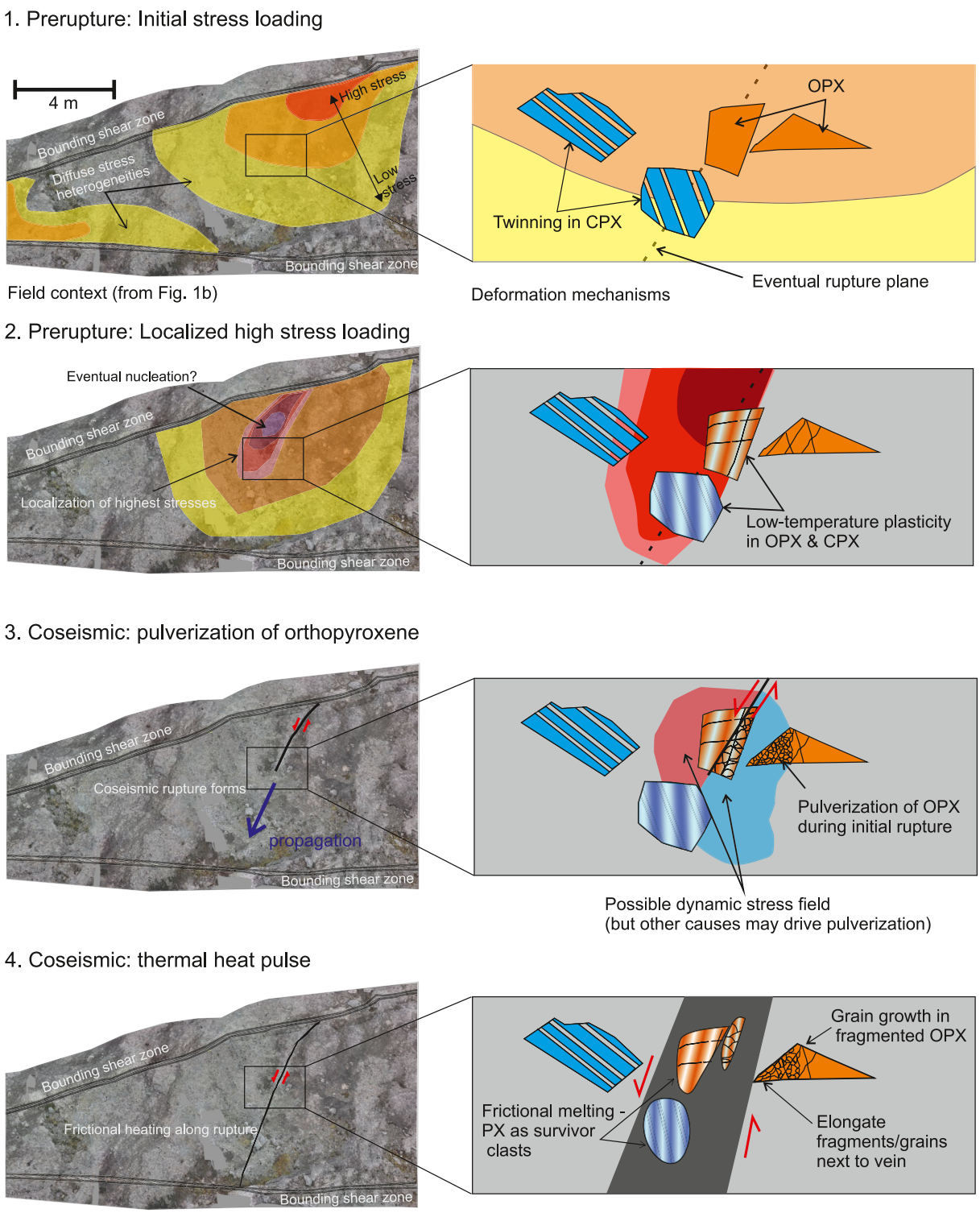

Figure 12. Proposed order and association of pyroxene microstructure and deformation processes with potential rupture processes. A conceptual example from the context of the shear-zone bounded block shown in Figure 1b—in this example, the prerupture stress loading is thought to be driven by the activity of the shear zones (Campbell et al., 2020).

4. After the passage of the rupture tip, frictional heating during continued earthquake slip melts phases along the fault plane, eventually cooling to form the pseudotachylyte vein. Fragments of pyroxene and plagioclase, sourced from the fault walls and comminuted material, may survive, unmelted, as clasts. Conduction of the

frictional heat pulse into the wall rock is a feasible driver of (oriented) grain growth within the fragmented orthopyroxene immediately adjacent to the pseudotachylyte vein.

6. Conclusions

Deformation mechanisms in both clinopyroxene and orthopyroxene spatially associated with ancient seismogenic faults from Nusfjord (Lofoten, Norway) record increasing localization of progressively higher stress (up to GPa in magnitude) prior to rupture, preceding pulverization-style fragmentation of orthopyroxene potentially linked to the passage of the rupture tip, or to alternative coseismic stress modifications. The spatial association of these microstructures with a single-slip pseudotachylyte-bearing fault plane, constrained to represent earthquake rupture nucleating at lower-crustal depths, implies that the sequence of overprinting microstructures may be linked to loading and eventual rupture during one lower crustal seismic cycle.

The extent to which low-temperature plasticity within lower crustal granulite can accommodate transient stress amplification may be an important control on when and where rupture and subsequent seismic damage can initiate within the lower crust. Intracrystalline deformation of phases along the fault plane and in the damage zone is an increasingly recognized and valuable record of the short-term changes to the stress regime prior to rupture in lower crustal rocks.

Data Availability Statement

Available data in support of this work include: unfiltered EBSD datasets, images used for grain size data analysis, spreadsheets showing calculations for grain size data analysis and grain growth modelling. These data are available at the British Geological National Geoscience Data Centre via https://webapps.bgs.ac.uk/services/ngdc/accessions/index.html#item169329 under a non-exclusive in-perpetuity licence.

Acknowledgments
This work was supported by the UK Natural Environment Research Council (grant NE/P001548/1 "The Geological Record of the Earthquake Cycle in the Lower Crust"). We thank colleagues at the Plymouth Electron Microscopy Centre for guidance and support with SEM analysis. We thank Scott Johnson, three anonymous reviewers and an Associate Editor of JGR for their constructive and thorough reviews, which have greatly improved the paper. Sample N22 was collected by Elliot Wood and Katherine Harris during their MGeol project at the University of Plymouth. Unfortunately, Elliot is no longer with us to see the completion of this work. This paper is dedicated to him, and to his passion for science and nature.

References

Aben, F. M., Doan, M.-L., Gratier, J.-P., & Renard, F. (2017). Coseismic damage generation and pulverization in fault zones. *Fault Zone Dynamic Processes*, 47–80. https://doi.org/10.1002/9781119156895.ch4

Aben, F. M., Doan, M.-L., Mitchell, T. M., Toussaint, R., Reuschlé, T., Fondriest, M., et al. (2016). Dynamic fracturing by successive coseismic loadings leads to pulverization in active fault zones. *Journal of Geophysical Research: Solid Earth*, *121*(4), 2338–2360. https://doi.org/10.1002/2015JB012542

Anderson, E. K., Song, W. J., Johnson, S. E., & Cruz-Uribe, A. M. (2021). Mica kink-band geometry as an indicator of coseismic dynamic loading. *Earth and Planetary Science Letters*, *567*, 117000. https://doi.org/10.1016/j.epsl.2021.117000

Aupart, C., Dunkel, K. G., Angheluta, L., Austrheim, H., Ildefonse, B., Malthe-Sørenssen, A., & Jamtveit, B. (2018). Olivine grain size distributions in faults and shear zones: Evidence for nonsteady state deformation. *Journal of Geophysical Research: Solid Earth*, *123*(9), 7421–7443. https://doi.org/10.1029/2018JB015836

Austrheim, H., Dunkel, K. G., Plümper, O., Ildefonse, B., Liu, Y., & Jamtveit, B. (2017). Fragmentation of wall rock garnets during deep crustal earthquakes. *Science Advances*, *3*(2). https://doi.org/10.1126/sciadv.1602067

Avé Lallemant, H. G. (1978). Experimental deformation of diopside and websterite. *Tectonophysics*, *48*(1), 1–27. https://doi.org/10.1016/0040-1951(78)90083-5

Bestmann, M., Pennacchioni, G., Nielsen, S., Göken, M., & de Wall, H. (2012). Deformation and ultrafine dynamic recrystallization of quartz in pseudotachylyte-bearing brittle faults: A matter of a few seconds. *Journal of Structural Geology*, *38*, 21–38. https://doi.org/10.1016/j.jsg.2011.10.001

Birtel, S., & Stöckhert, B. (2008). Quartz veins record earthquake-related brittle failure and short term ductile flow in the deep crust. *Tectonophysics*, *457*(1–2), 53–63. https://doi.org/10.1016/j.tecto.2008.05.018

Brückner, L. M., & Trepmann, C. A. (2021). Stresses during pseudotachylyte formation—Evidence from deformed amphibole and quartz in fault rocks from the Silvretta basal thrust (Austria). *Tectonophysics*, *817*, 229046. https://doi.org/10.1016/j.tecto.2021.229046

Brune, J. N. (2001). Fault-normal dynamic unloading and loading: An explanation for "non-gouge" rock powder and lack of fault-parallel shear bands along the San Andreas Fault. In *AGU fall meeting abstracts*. AGU.

Bystricky, M., & Mackwell, S. (2001). Creep of dry clinopyroxene aggregates. *Journal of Geophysical Research*, *106*(B7), 13443–13454. https://doi.org/10.1029/2001JB000333

Campbell, L., & Menegon, L. (2021). Electron backscatter diffraction data and sample analysis from the Nusfjord Shear Zone, Lofoten, Norway. Dataset. *NERC EDS National Geoscience Data Centre*. https://doi.org/10.5285/fc332502-1b15-48db-a4f0-16274e924ba0

Campbell, L. R., & Menegon, L. (2019). Transient high strain rate during localized viscous creep in the dry lower continental crust (Lofoten, Norway). *Journal of Geophysical Research: Solid Earth*, *124*(10), 10240–10260. https://doi.org/10.1029/2019JB018052

Campbell, L. R., Menegon, L., Fagereng, Å., & Pennacchioni, G. (2020). Earthquake nucleation in the lower crust by local stress amplification. *Nature Communications*, *11*(1), 1322. https://doi.org/10.1038/s41467-020-15150-x

Corfu, F. (2004). U–Pb age, setting and tectonic significance of the anorthosite–mangerite–charnockite–granite suite, Lofoten–Vesterålen, Norway. *Journal of Petrology*, *45*(9), 1799–1819. https://doi.org/10.1093/petrology/egh034

Doan, M.-L., & Gary, G. (2009). Rock pulverization at high strain rate near the San Andreas fault. *Nature Geoscience*, *2*(10), 709–712. https://doi.org/10.1038/ngeo640

Dohmen, R., Ter heege, J. H., Becker, H.-W., & Chakraborty, S. (2016). Fe-Mg interdiffusion in orthopyroxene. *American Mineralogist*, *101*(10), 2210–2221. https://doi.org/10.2138/am-2016-5815

Dor, O., Rockwell, T. K., & Ben-Zion, Y. (2006). Geological observations of damage asymmetry in the structure of the San Jacinto, San Andreas and punchbowl faults in southern California: A possible indicator for preferred rupture propagation direction. *Pure and Applied Geophysics*, *163*(2), 301–349. https://doi.org/10.1007/s00024-005-0023-9

Dorner, D., & Stöckhert, B. (2004). Plastic flow strength of jadeite and diopside investigated by microindentation hardness tests. *Tectonophysics*, *379*(1), 227–238. https://doi.org/10.1016/j.tecto.2003.11.008

Druiventak, A., Matysiak, A., Renner, J., & Trepmann, C. A. (2012). Kick-and-cook experiments on peridotite: Simulating coseismic deformation and post-seismic creep. *Terra Nova*, *24*(1), 62–69. https://doi.org/10.1111/j.1365-3121.2011.01038.x

Druiventak, A., Trepmann, C. A., Renner, J., & Hanke, K. (2011). Low-temperature plasticity of olivine during high stress deformation of peridotite at lithospheric conditions—An experimental study. *Earth and Planetary Science Letters*, *311*(3), 199–211. https://doi.org/10.1016/j.epsl.2011.09.022

Dunkel, K. G., Zhong, X., Arnestad, P. F., Valen, L. V., & Jamtveit, B. (2020). High transient stress in the lower crust: Evidence from dry pseudotachylytes in granulites, Lofoten Archipelago, northern Norway. *Geology*, *49*(2), 135–139. https://doi.org/10.1130/G48002.1

Ellis, S., & Stöckhert, B. (2004). Elevated stresses and creep rates beneath the brittle-ductile transition caused by seismic faulting in the upper crust. *Journal of Geophysical Research*, *109*(B5). https://doi.org/10.1029/2003JB002744

Ferrand, T. P., Hilairet, N., Incel, S., Deldicque, D., Labrousse, L., Gasc, J., et al. (2017). Dehydration-driven stress transfer triggers intermediate-depth earthquakes. *Nature Communications*, *8*(1), 15247. https://doi.org/10.1038/ncomms15247

Hacker, B. R., Peacock, S. M., Abers, G. A., & Holloway, S. D. (2003). Subduction factory 2. Are intermediate-depth earthquakes in subducting slabs linked to metamorphic dehydration reactions? *Journal of Geophysical Research*, *108*(B1), 2030. https://doi.org/10.1029/2001JB001129

Hagan, J. T. (1981). Impossibility of fragmenting small particles: Brittle—Ductile transition. *Journal of Materials Science*, *16*(10), 2909–2911. https://doi.org/10.1007/bf02402857

Hawemann, F., Mancktelow, N. S., Pennacchioni, G., Wex, S., & Camacho, A. (2019). Weak and slow, strong and fast: How shear zones evolve in a dry continental crust (Musgrave Ranges, Central Australia). *Journal of Geophysical Research: Solid Earth*, *124*(1), 219–240. https://doi.org/10.1029/2018JB016559

Incel, S., Schubnel, A., Renner, J., John, T., Labrousse, L., Hilairet, N., et al. (2019). Experimental evidence for wall-rock pulverization during dynamic rupture at ultra-high pressure conditions. *Earth and Planetary Science Letters*, *528*, 115832. https://doi.org/10.1016/j.epsl.2019.115832

Ingrin, J., Doukhan, N., & Doukhan, J.-C. (1992). Dislocation glide systems in diopside single crystals deformed at 800–900°C. *European Journal of Mineralogy*, *4*(6), 1291–1302. https://doi.org/10.1127/ejm/4/6/1291

Jamtveit, B., Ben-Zion, Y., Renard, F., & Austrheim, H. (2018). Earthquake-induced transformation of the lower crust. *Nature*, *556*(7702), 487–491. https://doi.org/10.1038/s41586-018-0045-y

Jamtveit, B., Petley-Ragan, A., Incel, S., Dunkel, K. G., Aupart, C., Austrheim, H., et al. (2019). The effects of earthquakes and fluids on the metamorphism of the lower continental crust. *Journal of Geophysical Research: Solid Earth*, *124*(8), 7725–7755. https://doi.org/10.1029/2018JB016461

Johnson, S. E., Song, W. J., Vel, S. S., Song, B. R., & Gerbi, C. C. (2021). Energy partitioning, dynamic fragmentation, and off-fault damage in the earthquake source volume. *Journal of Geophysical Research: Solid Earth*, *126*(11), e2021JB022616. https://doi.org/10.1029/2021jb022616

Kanagawa, K., Shimano, H., & Hiroi, Y. (2008). Mylonitic deformation of gabbro in the lower crust: A case study from the Pankenushi gabbro in the Hidaka metamorphic belt of central Hokkaido, Japan. *Journal of Structural Geology*, *30*(9), 1150–1166. https://doi.org/10.1016/j.jsg.2008.05.007

Keulen, N., Heilbronner, R., Stünitz, H., Boullier, A.-M., & Ito, H. (2007). Grain size distributions of fault rocks: A comparison between experimentally and naturally deformed granitoids. *Journal of Structural Geology*, *29*(8), 1282–1300. https://doi.org/10.1016/j.jsg.2007.04.003

Kidder, S., Hirth, G., Avouac, J.-P., & Behr, W. (2016). The influence of stress history on the grain size and microstructure of experimentally deformed quartzite. *Journal of Structural Geology*, *83*, 194–206. https://doi.org/10.1016/j.jsg.2015.12.004

Kim, J.-W., Ree, J.-H., Han, R., & Shimamoto, T. (2010). Experimental evidence for the simultaneous formation of pseudotachylyte and mylonite in the brittle regime. *Geology*, *38*(12), 1143–1146. https://doi.org/10.1130/g31593.1

Kirby, S. H., & Kronenberg, A. K. (1984). Deformation of clinopyroxenite: Evidence for a transition in flow mechanisms and semibrittle behavior. *Journal of Geophysical Research*, *89*(B5), 3177–3192. https://doi.org/10.1029/JB089iB05p03177

Kohlstedt, D. L., & Vander Sande, J. B. (1973). Transmission electron microscopy investigation of the defect microstructure of four natural orthopyroxenes. *Contributions to Mineralogy and Petrology*, *42*(2), 169–180. https://doi.org/10.1007/BF00371506

Kollé, J. J., & Blacic, J. D. (1982). Deformation of single-crystal clinopyroxenes: 1. Mechanical twinning in diopside and hedenbergite. *Journal of Geophysical Research*, *87*(B5), 4019–4034. https://doi.org/10.1029/JB087iB05p04019

Kollé, J. J., & Blacic, J. D. (1983). Deformation of single-crystal clinopyroxenes: 2. Dislocation-Controlled flow processes in hedenbergite. *Journal of Geophysical Research*, *88*(B3), 2381–2393. https://doi.org/10.1029/JB088iB03p02381

Küster, M., & Stöckhert, B. (1999). High differential stress and sublithostatic pore fluid pressure in the ductile regime —Microstructural evidence for short-term post-seismic creep in the Sesia Zone, Western Alps. *Tectonophysics*, *303*(1–4), 263–277. https://doi.org/10.1016/s0040-1951(98)00256-x

Lloyd, G. E., Farmer, A. B., & Mainprice, D. (1997). Misorientation analysis and the formation and orientation of subgrain and grain boundaries. *Tectonophysics*, *279*(1), 55–78. https://doi.org/10.1016/s0040-1951(97)00115-7

Mancktelow, N. S., Camacho, A., & Pennacchioni, G. (2022). Time-lapse record of an earthquake in the dry felsic lower continental crust preserved in a pseudotachylyte-bearing fault. *Journal of Geophysical Research: Solid Earth*, *127*(4), e2021JB022878. https://doi.org/10.1029/2021JB022878

Markl, G., Frost, B. R., & Bucher, K. (1998). The origin of anorthosites and related rocks from the Lofoten islands, northern Norway: I. Field relations and estimation of intrinsic variables. *Journal of Petrology*, *39*(8), 1425–1452. https://doi.org/10.1093/petroj/39.8.1425

Matysiak, A. K., & Trepmann, C. A. (2012). Crystal–plastic deformation and recrystallization of peridotite controlled by the seismic cycle. *Tectonophysics*, *530*, 111–127. https://doi.org/10.1016/j.tecto.2011.11.029

Menegon, L., Pennacchioni, G., Malaspina, N., Harris, K., & Wood, E. (2017). Earthquakes as precursors of ductile shear zones in the dry and strong lower crust. *Geochemistry, Geophysics, Geosystems*, *18*(12), 4356–4374. https://doi.org/10.1002/2017GC007189

Milke, R., Neusser, G., Kolzer, K., & Wunder, B. (2013). Very little water is necessary to make a dry solid silicate system wet. *Geology*, *41*(2), 247–250. https://doi.org/10.1130/G33674.1

Muto, J., Nakatani, T., Nishikawa, O., & Nagahama, H. (2015). Fractal particle size distribution of pulverized fault rocks as a function of distance from the fault core. *Geophysical Research Letters*, *42*(10), 3811–3819. https://doi.org/10.1002/2015gl064026

Ngo, D., Huang, Y., Rosakis, A., Griffith, W. A., & Pollard, D. (2012). Off-fault tensile cracks: A link between geological fault observations, lab experiments, and dynamic rupture models. *Journal of Geophysical Research*, *117*(B1), B01307. https://doi.org/10.1029/2011jb008577

Okudaira, T., Jeřábek, P., Stünitz, H., & Fusseis, F. (2015). High-temperature fracturing and subsequent grain-size-sensitive creep in lower crustal gabbros: Evidence for coseismic loading followed by creep during decaying stress in the lower crust? *Journal of Geophysical Research: Solid Earth*, *120*(5), 3119–3141. https://doi.org/10.1002/2014JB011708

Orlandini, O. F., & Mahan, K. H. (2020). Rheological evolution of a pseudotachylyte-bearing deep crustal shear zone in the western Canadian shield. *Journal of Structural Geology*, *141*, 104188. https://doi.org/10.1016/j.jsg.2020.104188

Orzol, J., Trepmann, C. A., Stöckhert, B., & Shi, G. (2003). Critical shear stress for mechanical twinning of jadeite—An experimental study. *Tectonophysics*, *372*(3), 135–145. https://doi.org/10.1016/s0040-1951(03)00242-7

Ostermeijer, G. A., Aben, F. M., Mitchell, T. M., Rockwell, T. K., Rempe, M., & Farrington, K. (2022). Evolution of co-seismic off-fault damage towards pulverisation. *Earth and Planetary Science Letters*, *579*, 117353. https://doi.org/10.1016/j.epsl.2021.117353

Papa, S., Pennacchioni, G., Angel, R. J., & Faccenda, M. (2018). The fate of garnet during (deep-seated) coseismic frictional heating: The role of thermal shock. *Geology*, *46*(5), 471–474. https://doi.org/10.1130/G40077.1

Papa, S., Pennacchioni, G., Menegon, L., & Thielmann, M. (2020). High-stress creep preceding coseismic rupturing in amphibolite-facies ultramylonites. *Earth and Planetary Science Letters*, *541*, 116260. https://doi.org/10.1016/j.epsl.2020.116260

Petley-Ragan, A., Ben-Zion, Y., Austrheim, H., Ildefonse, B., Renard, F., & Jamtveit, B. (2019). Dynamic earthquake rupture in the lower crust. *Science Advances*, *5*(7), eaaw0913. https://doi.org/10.1126/sciadv.aaw0913

Petley-Ragan, A., Dunkel, K. G., Austrheim, H., Ildefonse, B., & Jamtveit, B. (2018). Microstructural records of earthquakes in the lower crust and associated fluid-driven metamorphism in plagioclase-rich granulites. *Journal of Geophysical Research: Solid Earth*, *123*(5), 3729–3746. https://doi.org/10.1029/2017JB015348

Petley-Ragan, A. J., Plümper, O., Ildefonse, B., & Jamtveit, B. (2021). Nanoscale earthquake records preserved in plagioclase microfractures from the lower continental crust. *Solid Earth*, *12*(4), 959–969. https://doi.org/10.5194/se-12-959-2021

Pittarello, L., Di Toro, G., Bizzarri, A., Pennacchioni, G., Hadizadeh, J., & Cocco, M. (2008). Energy partitioning during seismic slip in pseudotachylyte-bearing faults (Gole Larghe Fault, Adamello, Italy). *Earth and Planetary Science Letters*, *269*(1–2), 131–139. https://doi.org/10.1016/j.epsl.2008.01.052

Platt, J. P., & Behr, W. M. (2011). Grainsize evolution in ductile shear zones: Implications for strain localization and the strength of the lithosphere. *Journal of Structural Geology*, *33*(4), 537–550. https://doi.org/10.1016/j.jsg.2011.01.018

Raleigh, C. B., & Talbot, J. L. (1967). Mechanical twinning in naturally and experimentally deformed diopside. *American Journal of Science*, *265*(2), 151–165. https://doi.org/10.2475/ajs.265.2.151

Reches, Z., & Dewers, T. A. (2005). Gouge formation by dynamic pulverization during earthquake rupture. *Earth and Planetary Science Letters*, *235*(1), 361–374. https://doi.org/10.1016/j.epsl.2005.04.009

Rowe, C. D., & Griffith, W. A. (2015). Do faults preserve a record of seismic slip: A second opinion. *Journal of Structural Geology*, *78*, 1–26. https://doi.org/10.1016/j.jsg.2015.06.006

Sibson, R. H. (1975). Generation of pseudotachylyte by ancient seismic faulting. *Geophysical Journal of the Royal Astronomical Society*, *43*(3), 775–794. https://doi.org/10.1111/j.1365-246X.1975.tb06195.x

Sibson, R. H., & Toy, V. G. (2006). The habitat of fault-generated pseudotachylyte: Presence vs. absence of friction-melt. In *Earthquakes: Radiated energy and the physics of faulting* (Vol. 170, pp. 153–166). AGU. https://doi.org/10.1029/170GM16

Skemer, P., & Karato, S. (2007). Effects of solute segregation on the grain-growth kinetics of orthopyroxene with implications for the deformation of the upper mantle. *Physics of the Earth and Planetary Interiors*, *164*(3), 186–196. https://doi.org/10.1016/j.pepi.2007.06.011

Soda, Y., & Okudaira, T. (2018). Microstructural evidence for the deep pulverization in a lower crustal meta-anorthosite. *Terra Nova*, *30*(6), 399–405. https://doi.org/10.1111/ter.12355

Song, B. R., Johnson, S. E., Song, W. J., Gerbi, C. C., & Yates, M. G. (2020). Coseismic damage runs deep in continental strike-slip faults. *Earth and Planetary Science Letters*, *539*, 116226. https://doi.org/10.1016/j.epsl.2020.116226

Song, W. J., Johnson, S. E., & Gerbi, C. C. (2020). Quartz fluid inclusion abundance and off-fault damage in a deeply exhumed, strike-slip, seismogenic fault. *Journal of Structural Geology*, *139*, 104118. https://doi.org/10.1016/j.jsg.2020.104118

Spray, J. G. (2010). Frictional melting processes in planetary materials: From hypervelocity impact to earthquakes. *Annual Review of Earth and Planetary Sciences*, *38*(1), 221–254. https://doi.org/10.1146/annurev.earth.031208.100045

Stünitz, H., Keulen, N., Hirose, T., & Heilbronner, R. (2010). Grain size distribution and microstructures of experimentally sheared granitoid gouge at coseismic slip rates—Criteria to distinguish seismic and aseismic faults? *Journal of Structural Geology*, *32*(1), 59–69. https://doi.org/10.1016/j.jsg.2009.08.002

Sullivan, W. A., & Peterman, E. M. (2017). Pulverized granite at the brittle-ductile transition: An example from the Kellyland fault zone, eastern Maine, USA. *Journal of Structural Geology*, *101*, 109–123. https://doi.org/10.1016/j.jsg.2017.07.002

Trepmann, C., & Stöckhert, B. (2001). Mechanical twinning of jadeite—An indication of synseismic loading beneath the brittle–plastic transition. *International Journal of Earth Sciences*, *90*(1), 4–13. https://doi.org/10.1007/s005310000165

Trepmann, C. A., Renner, J., & Druiventak, A. (2013). Experimental deformation and recrystallization of olivine-processes and timescales of damage healing during postseismic relaxation at mantle depths. *Solid Earth*, *4*(2), 423–450. https://doi.org/10.5194/se-4-423-2013

Trepmann, C. A., & Seybold, L. (2019). Deformation at low and high stress-loading rates. *Geoscience Frontiers*, *10*(1), 43–54. https://doi.org/10.1016/j.gsf.2018.05.002

Trepmann, C. A., & Stöckhert, B. (2002). Cataclastic deformation of garnet: A record of synseismic loading and postseismic creep. *Journal of Structural Geology*, *24*(11), 1845–1856. https://doi.org/10.1016/s0191-8141(02)00004-4

Trepmann, C. A., & Stöckhert, B. (2013). Short-wavelength undulatory extinction in quartz recording coseismic deformation in the middle crust; An experimental study. *Solid Earth*, *4*(2), 263–276. https://doi.org/10.5194/se-4-263-2013

Wilson, B., Dewers, T., Reches, Z., & Brune, J. (2005). Particle size and energetics of gouge from earthquake rupture zones. *Nature*, *434*(7034), 749–752. https://doi.org/10.1038/nature03433

Xu, S., & Ben-Zion, Y. (2017). Theoretical constraints on dynamic pulverization of fault zone rocks. *Geophysical Journal International*, *209*(1), 282–296. https://doi.org/10.1093/gji/ggx033

Yuan, F., Prakash, V., & Tullis, T. (2011). Origin of pulverized rocks during earthquake fault rupture. *Journal of Geophysical Research*, *116*(B6), B06309. https://doi.org/10.1029/2010JB007721